H4K20me3-Mediated Repression of Inflammatory Genes Is a Characteristic and Targetable Vulnerability of Persister Cancer Cells

Valentina Ramponi[1], Laia Richart[2], Marta Kovatcheva[1,3], Camille Stephan-Otto Attolini[1], Jordi Capellades[4,5], Alice E. Lord[6], Oscar Yanes[5,7], Gabriella Ficz[6], and Manuel Serrano[1,2]

ABSTRACT

Anticancer therapies can induce cellular senescence or drug-tolerant persistence, two types of proliferative arrest that differ in their stability. While senescence is highly stable, persister cells efficiently resume proliferation upon therapy termination, resulting in tumor relapse. Here, we used an ATP-competitive mTOR inhibitor to induce and characterize persistence in human cancer cells of various origins. Using this model and previously described models of senescence, we compared the same cancer cell lines under the two types of proliferative arrest. Persister and senescent cancer cells shared an expanded lysosomal compartment and hypersensitivity to BCL-XL inhibition. However, persister cells lacked other features of senescence, such as loss of lamin B1, senescence-associated β-galactosidase activity, upregulation of MHC-I, and an inflammatory and secretory phenotype (senescence-associated secretory phenotype or SASP). A genome-wide CRISPR/Cas9 screening for genes required for the survival of persister cells revealed that they are hypersensitive to the inhibition of one-carbon (1C) metabolism, which was validated by the pharmacologic inhibition of serine hydroxymethyltransferase, a key enzyme that feeds methyl groups from serine into 1C metabolism. Investigation into the relationship between 1C metabolism and the epigenetic regulation of transcription uncovered the presence of the repressive heterochromatic mark H4K20me3 at the promoters of SASP and IFN response genes in persister cells, whereas it was absent in senescent cells. Moreover, persister cells overexpressed the H4K20 methyltransferases KMT5B/C, and their downregulation unleashed inflammatory programs and compromised the survival of persister cells. In summary, this study identifies distinctive features and actionable vulnerabilities of persister cancer cells and provides mechanistic insight into their low inflammatory activity.

Significance: Cell persistence and senescence are distinct states of proliferative arrest induced by cancer therapy, with persister cells being characterized by the silencing of inflammatory genes through the heterochromatic mark H4K20me3.

See related commentary by Schmitt, p. 7

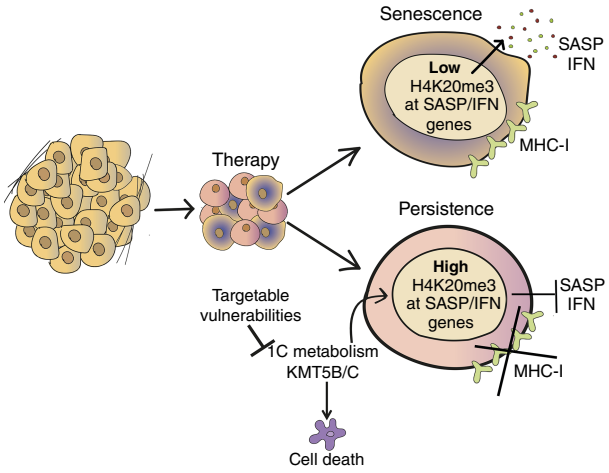

Introduction

Upon cancer therapy, a fraction of cancer cells often evade cell death by entering into a proliferative arrest and potentially contributing to tumor relapse (1). It is possible to distinguish at least two types of proliferative arrest in response to therapy: therapy-induced senescence (TIS), a state of low reversibility in which most cells remain arrested long-term, even upon therapy termination (2); and drug-tolerant persistence (DTP), a state in which cells can efficiently resume proliferation after removal of the anticancer drug (3). Persistence is closely related to the concept of dormancy in the context of metastasis (4). Metastatic cancer cells that settle in a nonpermissive tissue microenvironment may enter into a proliferative arrest known as dormancy that, reminiscent of drug persistence, can be reversed upon changes in the local microenvironment, such as the extracellular matrix or soluble factors (5, 6).

Extensive research on senescence has identified a number of cellular and molecular features frequently present in this form of cell-cycle arrest (7, 8). These include morphologic alterations

[1]Institute for Research in Biomedicine (IRB Barcelona), Barcelona Institute of Science and Technology (BIST), Barcelona, Spain. [2]Altos Labs, Cambridge Institute of Science, Granta Park, Cambridge, United Kingdom. [3]IFOM ETS - The AIRC Institute of Molecular Oncology, Milan, Italy. [4]Institut d'Investigació Sanitària Pere Virgili (IISPV), Reus, Spain. [5]CIBER de Diabetes y Enfermedades Metabólicas Asociadas (CIBERDEM), Instituto de Salud Carlos III, Madrid, Spain. [6]Centre for Haemato-Oncology, Barts Cancer Institute, John Vane Science Centre, Charterhouse Square, Queen Mary University of London, London, United Kingdom. [7]Department of Electronic Engineering, Universitat Rovira i Virgili, IISPV, Tarragona, Spain.

Corresponding Author: Manuel Serrano, Altos Labs, Cambridge Institute of Science, Granta Park, Cambridge CB21 6GP, United Kingdom. E-mail: mserrano@altoslabs.com

Cancer Res 2025;85:32–51

doi: 10.1158/0008-5472.CAN-24-0529

whereby cells become flattened and enlarged (9), expansion of the lysosomal compartment (10), increased activity of the lysosomal enzyme β-galactosidase (β-GAL; senescence-associated β-GAL or SA-β-GAL; ref. 11), high levels of reactive oxygen species (ROS; ref. 12), and significant alterations in chromatin structure, including loss of Lamin B1 (LMNB1) from the nuclear envelope, and the formation of senescence-associated heterochromatin foci (13–15). Together with their highly stable proliferative arrest, the most salient feature of senescent cells is their rich and robust secretory activity, known as the senescence-associated secretory phenotype (SASP), which includes cytokines, chemokines, and matrix remodeling proteins (16, 17). The SASP produced by intratumoral senescent cancer cells is partly responsible for the chemo-attraction of myeloid-derived suppressor cells and, thereby, for the exacerbation of immunosuppression postchemotherapy (2, 17, 18). Therefore, therapy-induced senescent cancer cells facilitate tumor relapse by promoting immunosuppression. The importance of TIS in disease progression is evidenced by multiple preclinical studies that have shown that drugs that selectively kill senescent cells, known as senolytics, improve the efficacy of standard chemotherapy (19, 20).

Compared with TIS, less is known about the molecular and cellular features of drug-tolerant persister cells. Recent studies have identified specific characteristics of persister cells, including slow cell cycle (21–25), elevated autophagy (24, 26), dependency on oxidative phosphorylation (27), altered epigenetic traits with increased repressive chromatin histone marks H3K9me3, H3K27me3 and decreased H3K4me3 (21, 23), a stem cell–like phenotype (22), and immune evasion (28). A remarkable recent finding has been the observation that cancer persister cells and embryonic diapause share extensive transcriptional overlap (24, 25). Embryonic diapause is a reversible state of suspended development, triggered by unfavorable nutrient conditions that can be mimicked in embryonic stem cells (ESC) *in vitro* using INK128, an ATP-competitive inhibitor of mTOR (bioRxiv 2023.05.29.541316; ref. 29). Embryonic diapause and INK128-induced ESC arrest are both efficiently reversed when nutrients are restored, or when the drug INK128 is removed, respectively. Based on this evidence, cancer drug-tolerant persister cells are also referred to as diapause-like cancer cells (24, 25), unifying diapause and persistence as a similar type of reversible proliferative arrest.

Here, we compare senescent and persister cells side by side to define shared and distinctive features. Through a genome-wide CRISPR/caspase-9 (Cas9) screen, we identify and validate genetic and pharmacologic vulnerabilities specific to persister cells and absent in senescent cells. Moreover, we uncover that persister cells, contrary to senescent cells, actively repress inflammatory programs, including the SASP, in a manner that is dependent on the heterochromatin mark H4K20me3 and its associated histone methyltransferases KMT5B/C. Collectively, our work highlights and defines distinctive features of drug-tolerant persister cells that are pharmacologically actionable for improved cancer control.

Materials and Methods

Cell lines and culture conditions

Human melanoma SK-Mel-147 (RRID: CVCL_3876), NSCLC A549 (RRID: CVCL_0023), H1299 (RRID: CVCL_0060), MCF7 (RRID: CVCL_0031), and MDA-MB-231 (RRID: CVCL_0062) cells were obtained from the ATCC. All the cell lines have been authenticated through a dedicated service provided by the Institute for Biomedical Research in Madrid. All the cell lines were maintained in standard DMEM (high glucose, Life Technologies, #12077579) supplemented with 10% heat inactivated FBS (Gibco, #10270106) and 1% anti–anti (Antibiotic-Antimycotic, Gibco, #15240062).

Mouse ESCs (mESC) were provided by Oscar Fernandez-Capetillo (CNIO, Madrid, RRID: SCR_014054). mESCs were grown on gelatin 1% with ES medium: DMEM (high glucose, Life Technologies, #12077579) supplemented with 15% FBS (Gibco, #10270106), 1% anti–anti (Antibiotic-Antimycotic, Gibco, #15240062), LIF (1,000 U/mL, Merck Millipore, #ESG1107), 0.1 mmol/L nonessential amino acids (Life Technologies, #11140035), 1% GlutaMAX (Life Technologies, #35050061), and 55 mmol/L β-mercaptoethanol (Merck, #M3148). Cells were passed every other day.

All cells were kept in a standard humidified incubator at 37°C and 5% CO_2. Cells were tested monthly for *Mycoplasma* contamination using standard PCR and only negative cells were used.

Induction of senescence

Senescence was induced by treatment with the DNA-damaging agent doxorubicin (100 nmol/L in all cell lines except MDA-MB-231 and H1299 50 nmol/L; Sigma, #D1515) or with the CDK4/6 inhibitor palbociclib (1 μmol/L in SK-Mel-147, H1299 and MCF7 cells and 5 μmol/L in A549 and MDA-MB-231 cells; PD033299, Absource Diagnostic, #S1116). After 3 days, cells were replenished with complete medium without the drugs. In A549 and MCF7 cells, palbociclib was maintained in the medium until cell collection. Cells were considered senescent 7 days after initiation of the treatment and analyzed or used for further treatments, as indicated.

Induction of persistence

Human cancer cells were treated with the dual mTOR/PI3K inhibitor INK128 (100 or 200 nmol/L; Abosurce Diagnostic, #S2811). mESCs were treated with INK128 (200 nmol/L) for 7 days. Medium was refreshed every 3 days including the inhibitor until cell collection, and the inhibitor was kept in the medium until cell collection.

siRNA transfection

All the siRNAs were purchased from siTOOLs. siRNAs have been used at 3 nmol/L final concentration. After 7 days from the beginning of the treatment to induce senescence or persistence, both proliferating, persister, and senescent SK-Mel-147 and A549 were transfected with siRNAs 5 days before performing viability assays. Lipofectamine reagent RNAiMAX (Life Technologies, #13778075) was used at 2 μL/mL diluted in Opti-MEM (Life Technologies, #31985062) to perform the transfection. Five days after the transfection, cell viability assays were performed, as indicated below.

Cell viability assays

Cell viability assays were performed in control proliferating or in cells undergoing senescence or persistence for 7 days. The following treatments were performed: navitoclax (1, 5 μmol/L; Eurodiagnostico, #HY-10087) for 3 days; (+)SHIN2 (100, 50 μmol/L; MedChemExpress, #HY-134978A) for 4 days; DL-Homocysteine (15, 5, 1.67 mmol/L; Sigma-Aldrich, #4628) for 3 days. The viable cell number was measured using CellTiter-Glo Luminescent Cell Viability Assay (Promega, #G7571) following manufacturer's instructions or Crystal Violet (Merck, #C6158). For CellTiter-Glo, raw

data were acquired by measuring luminescence in a VICTOR Multilabel Plate Reader (PerkinElmer, RRID: SCR_025714). For crystal violet staining, cells were first washed once with PBS and then fixed stained through the crystal violet solution (6 mmol/L crystal violet in 20% methanol solution in H_2O) for 30 minutes. The solution was then removed from the plates and cells were washed in H_2O at least 5 times and dry under a chemical hood overnight. Images were taken using an HP scanner. For quantification, the staining was lysed using lysing solution (0.1 mol/L sodium citrate and 50% ethanol at pH 4.2). Absorbance was measured using a Synergy HTX absorbance microplate reader (Agilent Technologies, RRID: SCR_019749) at 570 nm.

Gene expression analysis by qRT-PCR

Total RNA was extracted from cell samples using TRIzol reagent (Invitrogen, #15596018) or the RNeasy Micro Kit (Qiagen). Reverse transcription of up to 1 μg of total RNA was performed using the iScript cDNA Synthesis Kit (Bio-Rad, #1725038). qRT-PCR was performed using GoTaq PCR Master Mix (Promega, #A6002) and specific primers listed below. The reaction was performed in a QuantStudio 6 Flex thermocycler (Applied Biosystems, RRID: SCR_020239). All the reactions were performed in triplicates. *ACTB* and *GAPDH* were used as endogenous normalization controls, and all data were analyzed through the $2^{-\Delta\Delta CT}$ method. Primers sequences are listed in Supplementary Table S1.

Immunoblot

Cell pellets were lysed in 50 mmol/L Tris-HCl pH 7.4, 0.5% NP-40, 250 mmol/L NaCl, 5 mmol/L EDTA, with freshly added 1 mmol/L sodium orthovanadate, 1 mmol/L NaF, protease inhibitors (#87785, Thermo Fisher Scientific), and phosphatase inhibitors (#4906837001, Roche). Proteins (15 to 25 μg) were run on NuPAGE 4% to 12% gradient Bis-Tris gels in NuPAGE MES SDS Running Buffer (20×) and wet-transferred to 0.2 μmol/L nitrocellulose membranes (GE Healthcare, #10600001). Blots were blocked in Intercept (TBS) Blocking Buffer (LI-COR, #927-60001) for 30 minutes and then incubated with the following primary antibodies: rabbit anti–trimethyl-histone H3 (Lys9) antibody (1:500, Upstate, #07-442. RRID: AB_310620), rabbit anti–trimethyl-histone H4 (Lys20) antibody (1:500, Upstate, #07-749), rabbit anti–trimethyl-histone H4 antibody (1:500, Abcam, #ab9053, RRID: AB_306969), mouse anti–histone H4 antibody (1:500, Active Motif, #61521, RRID: AB_2793667), mouse anti–histone H3 (96C10) antibody (1:500, Cell Signaling Technology, #3638, RRID: AB_1642229), mouse anti–γ-tubulin antibody clone GTU-88 (1:5,000, Sigma, #T6557, RRID: AB_477584), rabbit anti–trimethyl-histone H3 (Lys4) antibody (1:500, Cell Signaling Technology, #9751S, RRID: AB_2616028), rabbit anti–trimethyl-histone H3 (Lys27) antibody (1:500, Upstate, #07-449, RRID: AB_310624), rabbit anti–monomethyl-histone H3 (Lys4) antibody (1:500, Invitrogen, #710795, RRID: AB_2532764) overnight. The following day the membranes were incubated with the following secondary antibodies: IRDye 800 CW anti-rabbit (1:5,000, LI-COR Odyssey, #926-32211, RRID: AB_621843) and IRDye 800 CW anti-mouse (1:5,000, LI-COR Odyssey, #926-32210, RRID: AB_621842).

Flow cytometry analysis

Cells were digested into single cells by trypsinization (0.25% trypsin-EDTA, Gibco, #25200056). For lysosomal mass measurement, cells were pretreated with LysoTracker dye (Invitrogen, Thermo Fisher Scientific, #L7528) according to manufacturer' instructions. Single cells were resuspended in FACS buffer (5 mmol/L EDTA and 0.5% BSA in PBS). For apoptosis detection, cells were stained with Annexin-V and Propidium Iodide Apoptosis Detection Kit (Thermo Fisher Scientific, #88-8007-74) according to manufacturer's instructions. For ROS detection, cells were stained with ROS detection solution from the ROS-ID Total ROS detection kit (Enzo Life Sciences, #ENZ-51011) according to manufacturer's instructions. For blocking, cells were incubated in FACS buffer with 20% FBS for 10 minutes at 4°C. Cells were stained with HLA-A, B, and C antibody (1:100, BioLegend, #311404, RRID: AB_314873) for 40 minutes. Cell viability was assessed using propidium iodide (PI, Sigma, #P4864) or Live/Dead Fixable Yellow dye (Invitrogen, #L34967), following the manufacturer's instructions. Cells were washed once with FACS buffer and run on a Gallios Beckman Coulter flow cytometer (BD Biosciences, RRID: SCR_019639) or a FACSAria Fusion (BD Biosciences, RRID: SCR_025715). The autofluorescence signal from unstained samples was obtained and subtracted from each stained sample in all experiments. Data were analyzed using FlowJo v10 software.

Cell-cycle analysis

Cells were digested into single cells by trypsinization (0.25% trypsin-EDTA, Gibco, #25200056) and resuspended at a concentration of 10^6 cells/mL in a solution of 30% PBS and 70% ice-cold EtOH for fixation. After at least 2 hours of fixation on ice, cells were resuspended in the following staining solution: 3% PI 500 μg/mL in sodium citrate 38 mmol/L (in water) and 3% RNAse A 10 mg/mL (Life Technologies, #EN0531) in PBS-EDTA 5 mmol/L at 4°C. Cells were analyzed by flow cytometry the day after.

SA-β-GAL staining

After one wash in PBS, cells were fixed in the SA-β-GAL fixing solution (5 nmol/L EGTA, 2 mmol/L $MgCl_2$, and 0.2% glutaraldehyde in 0.1 mol/L phosphate buffer) for 15 minutes at room temperature. After washing once with PBS, cells were incubated overnight at 37°C in SA-β-GAL staining solution pH 6 (40 mmol/L citric acid, 5 mmol/L potassium cyanoferrate (II) and (III), 150 mmol/L sodium chloride, and 2 mmol/L magnesium chloride, dissolved in 0.1 mol/L phosphate buffer containing 1 mg/mL X-Gal [Melford BioLaboratories, #MB1001) prepared in dimethylformamide (Sigma, #D4551)]. Cells were then washed once with PBS and kept in glycerol solution 0.5%. Pictures were taken using a Nikon Eclipse TS2 brightfield microscope (RRID: SCR_025716).

Immunofluorescence

Cells were fixed in 4% paraformaldehyde for 10 minutes, permeabilized in 0.2% Triton X-100, and blocked in 5% FBS and 0.2% Triton X-100. Primary antibodies (rabbit anti–trimethyl-histone H3 (Lys9) antibody (1:500, Upstate, #07-442) and rabbit anti–trimethyl-histone H4 (Lys20) antibody (1:500, Upstate, #07-749) were diluted in blocking solution and incubated over night at 4°C. Cells were washed 3 times with blocking solution for a total of 20 minutes and then incubated with secondary antibody (1:500, Invitrogen, #A31572, RRID: AB_162543) for 2 hours. Cells were washed twice with permeabilization buffer and mounted with VECTASHIELD Antifade Mounting Medium with 4′,6-diamidino-2-phenylindole (DAPI; Vector Laboratories, #H1200). For lysotracker staining, cells were incubated with LysoTracker dye (Invitrogen, Thermo Fisher Scientific, #L7528) according to manufacturer' instructions for 30′, before fixation in 4% paraformaldehyde. Confocal images were taken using the super-resolution Airyscan detector of ZEISS Elyra 7 microscope (RRID: SCR_025701) at ×100 and ×64 magnification

or with the Leica SP5 Spectral Confocal Multiphoton (RRID: SCR_020233) at ×64 magnification.

RNA sequencing

Total RNA was extracted using TRIzol reagent and the Rneasy Mini Kit (Qiagen, #QIA74106), following manufacturer's instructions. Total RNA extractions were quantified with a NanoDrop One (Thermo Fisher Scientific, RRID: SCR_023005), and RNA integrity was assessed with the Bioanalyzer 2100 RNA Nano assay (Agilent, RRID: SCR_019715). Libraries for RNA sequencing (RNA-seq) were prepared at Institute for Research in Biomedicine Barcelona Functional Genomics Core Facility (RRID: SCR_011301). Briefly, mRNA was isolated from 1.2 μg of total RNA and used to generate dual-indexed cDNA libraries with the Illumina stranded mRNA ligation kit (Illumina) and UD Indexes Set A (Illumina). Ten cycles of PCR amplification were applied to all libraries. Sequencing-ready libraries were quantified using the Qubit dsDNA HS assay (Invitrogen) and quality controlled with the Bioanalyzer 2100 DNA HS assay (Agilent, RRID: SCR_019715). An equimolar pool was prepared with the 32 libraries for SE75 sequencing on a NextSeq550 (Illumina, RRID: SCR_016384). Sequencing output was above 1,015 million 75-nt long single-end reads, and a minimum of 27.7 million reads were obtained for all samples. Adapters and low-quality bases (<Q20) were removed from single-end reads with Cutadapt (v4.4; RRID: SCR_011841) and TrimGalore (v0.6.10; RRID: SCR_011847; https://github.com/FelixKrueger/TrimGalore). Trimmed reads were then mapped to the human reference genome hg38 using the STAR (v2.7.10b; RRID: SCR_004463) aligner and the corresponding gene annotation from GENCODE: release 43/GRCh38.p13 (RRID: SCR_014966). The following parameters were used for mapping of RNA-seq reads against the reference genome: –outFilterMultimapNmax 1 –outFilterMismatchNmax 999 –seedSearchStartLmax 50 –outFilterScoreMinOverLread 0.66 –quantMode GeneCounts –alignEndsType Local. Differential expression analyses were conducted with DESeq2 (RRID: SCR_015687). Lists of genes preranked according to their $\log_2$ fold change between experimental conditions were submitted to gene set enrichment analysis (GSEA) to test for differential enrichment of GSEA hallmark and in-house SASP gene sets. Annotations of repetitive elements from the Repeat masker database in the human genome were downloaded from USCS (http://hgdownload.soe.ucsc.edu/goldenPath/mm10/database/) and converted to saf format. The featureCounts function was used to generate a count matrix for the annotated regions. Comparisons between conditions were performed using the DESeq2 package. Repetitive elements were grouped according to their family, as annotated in the original database.

CRISPR/Cas9 short-guide RNA screening

To perform the genome-wide screen, we used a CRISPR/Cas9 system previously described (30). ESCs were generated from mice ubiquitously expressing *Cas9* under control of the endogenous *Cola1a* locus and a tetracycline responsive operator transgene; reverse tetracycline-controlled transactivator synthesis is under control of the endogenous *ROSA26* locus. ESCs from these mice were infected with a lentiviral library encoding short-guide RNAs (sgRNA) targeting 19,150 mouse genes, with approximately five independent sgRNAs per gene. The addition of doxycycline to the ESCs causes inducible expression of the Cas9 enzyme, which induces editing of the sgRNA targets.

Diapause was induced in mESC through the mTOR/PI3K inhibitor INK128 at 200 nmol/L. After 5 days, half of the proliferating cells and half of the diapause cells were sequenced to know the initial diversity of the sgRNA library. Doxycycline was added to the remaining cells for 3 additional days to induce sgRNA editing before sequencing. Genomic DNA (gDNA) was isolated from cell pellets using a gDNA isolation kit [Blood & Cell Culture Midi kit (Qiagen)]. After gDNA isolation, sgRNAs were amplified and barcoded by PCR, to amplify the DNA fragment containing sgRNA sequences. PCR products were sequenced on a HiSeq 4000 instrument (Illumina, RRID: SCR_016386) at 50 bp reads to a depth of 30 mol/L reads per sample.

Reads were preprocessed by removing adapters using Cutadapt v4.1 (RRID: SCR_011841) with parameters "-e 0.2 -a GTTTTAGAGCTAGAAATAGCAAGTTAAAATA -m 18". Next sequences were trimmed to length 19 to match that of the probes. An artificial genome was created for alignment with Bowtie v0.12.9 (RRID: SCR_005476) using the probes' sequences and the function bowtie-build with default parameters. Finally, reads were aligned to this genome with parameters -S -t -p 20 -n 1 -l 19. Read counts were imported into R by reading the sam files and counting the number of occurrences of each probe. The resulting count matrix was normalized using the rlog function from the DESeq2 v1.34.0 R package (RRID: SCR_015687). A linear model with random and fixed effects was fitted to the normalize probe data for each gene. The condition was used as a fixed covariable whereas the guides were included as random effects whenever there was more than one. The model was fit with the function lmer from the lme4 package or with the native R lm function if there was only one probe for a given gene. Contrast coefficients and *P* values were computed using the glht function from the multcomp package without any *P* value adjustment.

Gene Ontology (GO) set collections were downloaded from http://geneontology.org. Genes quantified in the microarray study were annotated according to the Broad Hallmark (https://www.gsea-msigdb.org/gsea/msigdb). Functional enrichment analyses were performed using a modification of ROAST, a rotation-based approach implemented in the Limma R package, which is especially suitable for small experiments. Such modifications were implemented to accommodate the proposed statistical restandardization in the ROAST algorithm, which enables its use for competitive testing. The MaxMean statistic was used for testing gene set enrichment of the different gene collections. For each gene, the most variable guide within each gene was used in these analyses (median absolute deviation). The results of these analyses were adjusted by multiple comparisons using the Benjamini–Hochberg FDR method. All these were performed using the functions of the roastgsa R package.

Mass spectrometry analysis

Cells were mixed with 25 μL of tris(2-carboxyethyl)phosphine and 70 μL of 1% formic acid in methanol. Samples were vortexed and left in the freezer for 1 hour, centrifuged for 10 minutes at 12,000 rpm and 4°C, and transferred to glass vials for their analysis by LC-MS. LC/MS was performed with a Thermo Fisher Scientific Vanquish Horizon UHPLC System (RRID: SCR_025713) interfaced with a Thermo Fisher Scientific Orbitrap ID-X Tribrid Mass Spectrometer (RRID: SCR_025712).

Metabolites were separated by hydrophilic interaction liquid chromatography (HILIC) with an InfinityLab Poroshell 120 HILIC-Z (2.1 × 100 mm, 2.7 μm) column (Agilent Technologies). The mobile phase A was 50 mmol/L ammonium acetate in water, and mobile phase B was acetonitrile. Separation was conducted under the following gradient: 0 to 1 minute, isocratic 90% B; 1 to 6 minutes

decreased to 60% B; 6 to 6.2 minutes decreased again to 50% B; 6.2 to 7 minutes, isocratic 50% B; 7 to 7.2 minutes, increased to 90% B; 7.2 to 10.5 minutes, reequilibration column 90% B. The flow was 0.4 mL $minutes^{-1}$. The injection volume was 5 μL.

The mass spectrometry parameters used were as follows: isolation window (m/z), 2; spray voltage, 3,500 V; sheath gas, 50; auxiliary gas, 10; ion transfer tube temperature, 300°C; vaporizer temperature, 300°C; Orbitrap resolution, 7,500; RF Lens (%), 60; AGC target, 2e5; maximum injection time, 200 ms.

Cleavage Under Targets and Tagmentation sequencing

Cleavage Under Targets and Tagmentation (CUT&Tag) sequencing was performed at the Barts Cancer Institute (Queen Mary, University of London, RRID: SCR_011488), following the published protocol: https://www.protocols.io/view/bench-top-cut-amp-tag-kqdg34qdpl25/v3. The reagents used are listed in Supplementary Table S2. The indexed primers used for library preparation are listed in Supplementary Table S3.

Adapters and low-quality bases (<Q20) were removed from reads with Cutadapt (v4.4; RRID: SCR_011841) and TrimGalore (v0.6.10; RRID: SCR_011847; https://github.com/FelixKrueger/TrimGalore). Trimmed reads were mapped to the human reference genome hg38 with Bowtie2 (v2.5.1; RRID: SCR_016368) using default parameters. PCR duplicates were removed with Picard Tools MarkDuplicates (v1.97). Deduplicated bam files of biological replicates were merged using SAMtools (v1.6; RRID: SCR_002105) merge.

BigWig files were created using DeepTools (RRID: SCR_016366) bamCoverage (v3.0.2) with the following parameters: –normalizeUsingRPKM –ignoreForNormalization chrX chrY –samFlagInclude 64 –extendReads –binSize 20 –smoothLength 40. Reads overlapping problematic, blacklisted regions (hg38-blacklist.v2.bed) were excluded from the computation of coverage with the option –blackListFileName. In addition to scaling by library size, in order to remove any composition biases, we calculated a normalizing factor using the BioconductoR (RRID: SCR_006442) csaw::normFactors function. This function counts reads in 10-kb genome-wide nonoverlapping bins and uses the trimmed mean of M-values method to correct for any systematic fold change in the coverage of bins. The normalization factor was passed onto DeepTools bamCoverage with the parameter –scaleFactor.

Chromatin hidden Markov model (ChromHMM; RRID: SCR_018141) was used to identify chromatin fragments with differential enrichment for H3K9me3 and/or H4K20me3 between experimental conditions. The genome was analyzed at 500-bp intervals and a model of nine states was chosen to characterize both A549 and SK-Mel-147 cells. Two ChromHMM states were not included in downstream analyses because they showed no enrichment for neither H3K9me3 or H4K20me3. Genes were assigned to a ChromHMM state according to the percentage of overlap of their promoter regions, defined as TSS ± 3kb. Enrichment of ChromHMM states for GSEA hallmark gene sets was assessed using a hypergeometric test.

pA-Tn5 protein production

To produce double-stranded adaptors with 19mer Tn5 mosaic ends, single-stranded DNA oligos were ordered (Eurofins). The oligos' sequences are listed in Supplementary Table S4.

Oligos were resuspended to 200 μmol/L in annealing buffer (10 mmol/L Tris pH 8, 50 mmol/L NaCl, and 1 mmol/L EDTA). To produce double-stranded adapters, 20 μL Me-Rev and 20 μL Me-A were mixed and 20 μL Me-Rev and 20 μL Me-B were mixed. Tubes were placed in a thermocycler and incubated at 95°C for 2 minutes. After the initial incubation, the temperature was reduced by 5°C every 5 minutes until the final 5 minutes at 25°C. The 3xFLAG-pA-Tn5 purified protein with a concentration of 5.5 μmol/L (50% glycerol) was a kind gift from Chema Martin Lab (QMUL). To assemble the pA-Tn5 adapter transposome, 100 μL fusion protein was mixed with 10 μL pre-annealed Tn5MEDS-A (200 μmol/L) and 10 μL Tn5MEDS-B (200 μmol/L) oligonucleotides, and incubated at room temperature for 50 minutes. A loaded transposome was produced with a final glycerol concentration of 43%. The transposome was stored at −20°C until *in vitro* enzymatic activity assay or CUT&Tag experiment. pA-Tn5 transposome was incubated with 150 ng HMW Lambda DNA (NEB) in digestion buffer (5XTAPS-MgCl2-PEG8000) at 55°C for 7 minutes, prior to incubation with 1% SDS and proteinase K (20 mg/mL, NEB) to inactivate and degrade pA-Tn5. Samples were kept on ice and run on a 0.7% 1 × TBE agarose gel. Active pA-Tn5 transposome digested high molecular weight DNA and produced a smear on the agarose gel. Gel was imaged using UV-fluorescence on Chemidoc (Amersham Imager 600RGB).

Animal experimentation

Mouse experiments were performed at the Institute for Research in Biomedicine according to protocols approved by the Science Park of Barcelona Ethics Committee for Research and Animal Welfare. Animals were purchased from Envigo Spain and were housed in strict animal husbandry facilities free of specific pathogens and micro-organisms. The facilities had a controlled temperature environment and maintained normal 12-hour day–night light cycles. Mice were randomly selected for the peptide or vehicle treatment and placed in four cages with four animals each. Each cage had bedding to provide shelter and privacy as well as unlimited access to food and water. Animals were inspected daily by the qualified personnel and weekly or as needed by the institute's veterinary doctor.

SK-Mel-147 cells were digested into single cells by trypsinization (0.25% trypsin-EDTA, Invitrogen). Cells were resuspended at a concentration of 10^6 cells/100 μL in a solution of Matrigel (Corning Life Sciences, #354230) and DMEM (1:5) and subcutaneously injected in both flanks of athymic nude mice. When the tumors reached a size of approximately 75 to 100 mm^3, the mice were randomly divided in groups of four mice for each type of treatment.

Palbociclib (100 mg/kg in 50 mmol/L sodium lactate; Ambeed, #A295334), BEZ235 (35 mg/kg in a solution of PEG400 and PHOSAL 50 PG 1:2; Medchemtronica, #HY-50673), and navitoclax (50 mg/kg in a solution of PEG400 and PHOSAL 50 PG 1:2) were administered by oral gavage every day for 10 days; for combined treatments, navitoclax administration started 2 days after palbociclib and BEZ235. Xenograft tumors were measured every day using a digital caliper. Tumor volume was calculated using the formula: volume = $a \times b^2 \times 0.5$, in which "a" is the length, and "b" is the measured breadth of the tumor lump (skin included). Animals were sacrificed after 10 days from the beginning of the treatment or when tumors reached the size of 1,000 mm^3.

Statistical analysis

Data were analyzed using GraphPad Prism v.9.3.0 software and are represented as mean ± SEM of independent biological replicates. Statistical analyses were performed as described in the figures. Differences were considered significant based on P values (*, $P < 0.05$; **, $P < 0.01$; ***, $P < 0.001$; ****, $P < 0.0001$).

Data availability

The data generated in this study are publicly available in Gene Expression Omnibus at GSE246690 (RNA-seq), GSE251714 (sgRNA sequencing), and GSE251660 (CUT&Tag sequencing). Other data analyzed in this study were reported in ref. 24 and obtained from Gene Expression Omnibus at GSE145356. All other raw data are available upon request from the corresponding author.

Results

Inhibition of mTOR with INK128 induces persistence in cancer cells

Previous investigators have reported that persistence induced by standard chemotherapeutic drugs, such as irinotecan and docetaxel, shares similarities with embryonic diapause induced by nutrient deprivation or by the ATP-competitive mTOR inhibitor INK128 (24, 25). We wondered if INK128 would also induce a persistence/diapause-like state in cancer cells. For this, we tested human cancer cell lines of different origins, with the aim of capturing general features: melanoma SK-Mel-147, lung cancer A549, H1299, and H226, and breast cancer MCF7 and MDA-MB-231. All tested cell lines underwent a profound suppression of proliferation upon treatment with INK128 for 7 days (**Fig. 1A** and **B**; Supplementary Fig. S1A and S1B). Analysis of DNA content indicated that INK128-induced arrest occurred primarily at the G1 phase of the cell cycle (Supplementary Fig. S1C). Having shown the general ability of INK128 to induce growth arrest in multiple cancer cell lines, we decided to focus the large majority of our subsequent analyses on SK-Mel-147 and A549 cells, two cell lines of different origin (melanoma and lung, respectively) whose TIS phenotype has been extensively characterized (please note that in previous publications from our group, SK-Mel-147 cells were incorrectly identified as SK-Mel-103 until the recent publication of the STR profile of these cell lines at http://cellosaurus.org; refs. 31–34). Forty-eight hours of INK128 treatment was not toxic to cells, as Annexin V/PI staining did not detect apoptotic (Annexin V+ PI+) cells; after 7 days (with fresh medium every 2–3 days in the continuous presence of the drug), INK128-treated cells presented a modest increase in the number of apoptotic cells (from ≤2% in proliferating cells to ≤4% in INK128-treated cells; Supplementary Fig. S1D). Importantly, upon removal of INK128, cultures resumed proliferation (**Fig. 1A** and **B**; Supplementary Fig. S1B), thereby recapitulating a key feature of the persistence/diapause-like state, namely, its efficient reversibility (3). To address the potential emergence of INK128-resistant cells within the time frame of our assays, we maintained SK-Mel-147 cells in the presence of INK128 for 30 days, with no evidence of proliferation (Supplementary Fig. S1E). Furthermore, after three on/off cycles, cells remained responsive to INK128-induced arrest (Supplementary Fig. S1E). INK128-arrested cells were also more resistant to an unrelated drug, such as doxorubicin (Supplementary Fig. S1F), which is another feature of persistence (1). As mentioned in the Introduction, persistence shares similarities with cancer cell dormancy and we observed that INK128-arrested cells upregulated two well-known markers of cancer dormancy, *DEC2* (also known as *BHLHE41*) and *p27* (*CDKN1B*; **Fig. 1C**; Supplementary Fig. S1G; refs. 35, 36).

An important feature of cancer persister cells is the presence of a diapause-specific transcriptional program (bioRxiv 2023.05.29.541316; ref. 29). To explore if this was also the case of INK128-arrested cancer cells, we performed RNA-seq of SK-Mel-147 and A549 cells untreated or treated with INK128 for 7 days. GSEA revealed that INK128 induced the upregulation of the TGFβ and WNT/β-catenin pathways (**Fig. 1D**), both of which have been previously linked to tumor dormancy (36, 37). We also observed downregulation of the mTOR pathway and the unfolded protein response, which is consistent with the inhibition of mTOR and a reduction in protein synthesis (**Fig. 1D**). Similarly, the cell-cycle pathways and MYC target pathways were also downregulated, which are hallmarks of embryonic diapause (38). We then asked if the previously reported signatures of embryonic diapause (a signature of downregulated genes and a signature of upregulated genes; ref. 24) were also present in INK128-arrested cancer cells. Interestingly, both signatures were scored with high statistical significance in SK-Mel-147 and A549 cells treated with INK128 (**Fig. 1E**; Supplementary Fig. S1H). In a reciprocal exercise, we used the A549 and SK-Mel-147 transcriptomes to generate INK128 signatures of downregulated and upregulated genes (Supplementary Tables S5 and S6) and we compared them against previously published RNA sequencing datasets of persistence in colorectal cancer cells (24). In the case of colorectal cancer treated with chemotherapy, intratumoral fibroblasts may undergo senescence (39) whereas cancer cells may undergo persistence (24). Interestingly, our INK128 signatures scored significantly in the cancer cells of patient-derived xenografts (PDX) treated with irinotecan and undergoing persistence (DTP; **Fig. 1F**). In contrast, the INK128 signatures were absent in untreated PDX, in PDX in which the irinotecan treatment had been interrupted (recovery), and in PDX treated with irinotecan but with inherent resistance to the drug (resistant; **Fig. 1F**). Collectively, these data indicate that ATP-competitive mTOR inhibition in cancer cells induces persistence.

Shared features between persister and senescent cancer cells

We next wanted to compare side by side, using the same cellular models, the two types of proliferative arrest induced by therapy, namely, persistence (which is efficiently reversible) and senescence (which is inefficiently reversible). We used two different triggers of senescence, doxorubicin (a genotoxic agent) and palbociclib (a targeted therapy that inhibits the CDK4/6 kinases) in SK-Mel-147 and A549 cells. Senescence was confirmed by SA-β-GAL staining (see further below) and by an elevated lysosomal content (**Fig. 2A**; Supplementary Fig. S2A; refs. 10, 11, 31, 40, 41). Persister cells induced with INK128 also presented an increased lysosomal mass compared with proliferating cancer cells (**Fig. 2A**; Supplementary Fig. S2A). These results were confirmed in additional cancer cell lines (MCF7, MDA-MB-231, and H1299; Supplementary Fig. S2B).

A general feature of senescent cells is their high sensitivity to inhibitors of the antiapoptotic BCL2 family proteins and, in particular, to navitoclax, an inhibitor of BCL2, BCL-XL (encoded by *BCL2L1* gene), and BCL-W (encoded by *BCL2L2*; ref. 42). We wondered whether INK128-persister cells would share this feature with senescent cells. Proliferating, persister, and senescent SK-Mel-147 and A549 cells were treated with navitoclax for 48 hours and cell viability was assessed. As expected, senescent cells were sensitive to navitoclax, whereas proliferating cells were not (**Fig. 2B**; Supplementary Fig. S2C). Interestingly, INK128-persister cancer cells were also sensitive to navitoclax (**Fig. 2B**; Supplementary Fig. S2C). The protein levels of BCL2, BCL-W, and BCL-XL were not dramatically changed in senescent or persister cells compared with proliferating cells, although senescent cells presented a moderate increase in BCL-XL (**Fig. 2C**; Supplementary Fig. S2D), indicating that sensitivity to BCL2-family inhibition is not dictated by changes

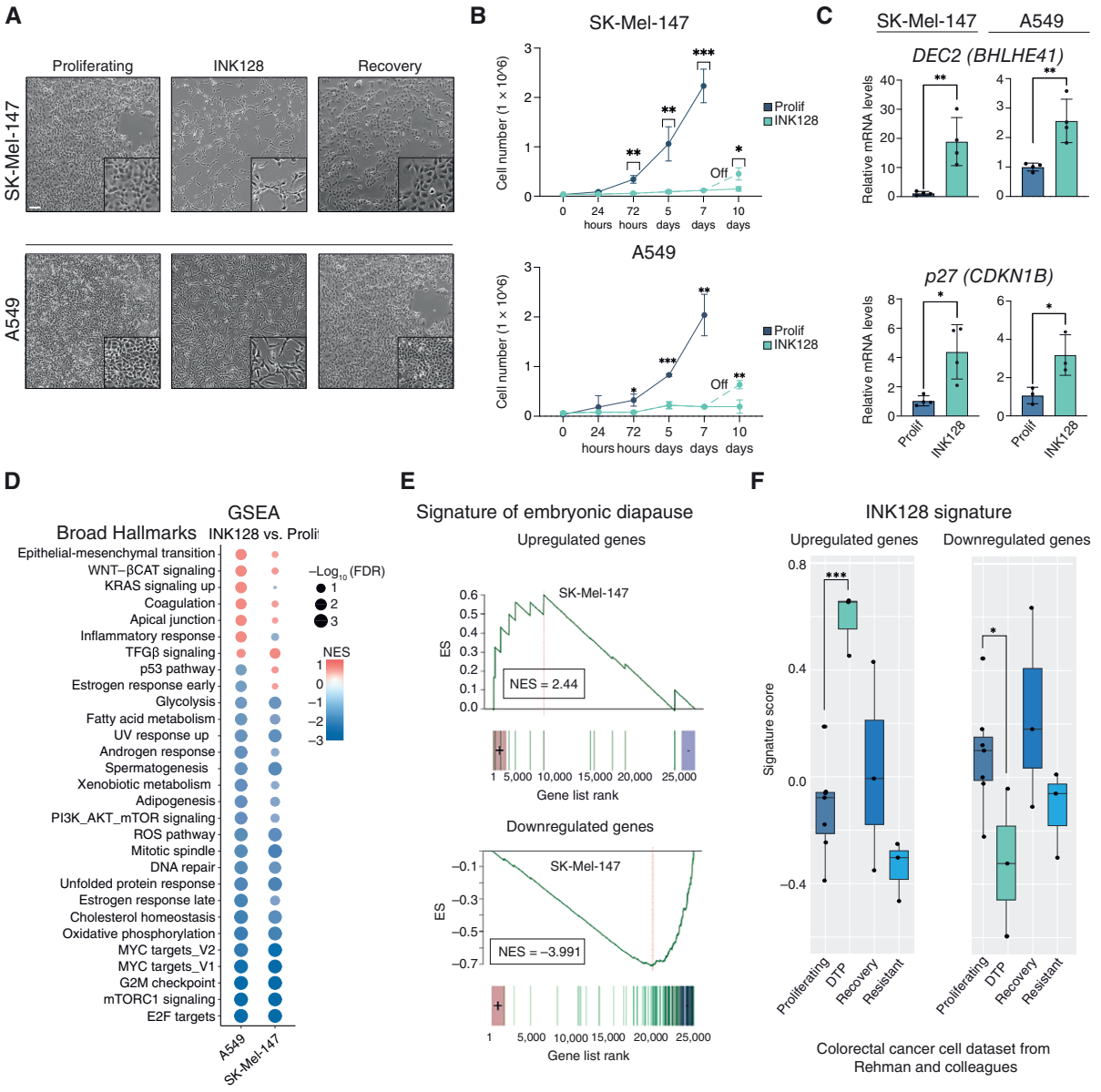

Figure 1.

INK128-treated cells undergo a reversible cell-cycle arrest with features of persistence and embryonic diapause. **A,** Brightfield pictures of SK-Mel-147 and A549 cells untreated (proliferating), treated with INK128 (100 and 200 nmol/L, respectively) for 7 days, and after INK128 withdrawal for 3 days. Scale bar, 100 μm. **B,** Proliferation curve of SK-Mel-147 and A549 cells untreated (proliferating), treated with INK128, and after INK128 withdrawal ($n = 3$). Cells were counted using a hemocytometer after 24 hours from plating, 3, 5, 7, and 10 days (or 3 days after INK128 withdrawal; $n = 3$). *, $P < 0.05$; **, $P < 0.01$; ***, $P < 0.001$; multiple unpaired Student *t* test. **C,** mRNA expression levels of *DEC2* (*BHLHE41*) and *p27* (*CDKN1B*) in untreated (proliferating) and INK128-treated SK-Mel-147 and A549 cells, measured by qRT-PCR (relative to the average expression of housekeeping genes *ACTB* and *GAPDH*). *, $P < 0.05$; **, $P < 0.01$; unpaired Student *t* test, compared with proliferating controls ($n = 3$ or 4). **D,** GSEA of INK128-treated SK-Mel-147 and A549 cells in comparison to untreated (proliferating) controls. Normalized enrichment score (NES) is color-coded, whereas statistical significance (FDR) is encoded in the size of the dots. **E,** GSEA of a signature of embryonic diapause, on the left genes upregulated in diapause and on the right genes downregulated in diapause. The signatures were analyzed in INK128-treated vs. proliferating SK-Mel-147 cells. **F,** Signature scores of control proliferating cells, DTP in response to irinotecan, cells that had exited persistence upon withdrawal of irinotecan (recovery), and cells that were resistant to irinotecan and did not undergo DTP (resistant; published datasets from Rehman and colleagues, ref. 24), when interrogated for the expression of the INK128 downregulated signature and the INK128 upregulated signature (proliferating $n = 8$; all the other conditions $n = 3$). *, $P < 0.05$; ***, $P < 0.001$; one-way ANOVA compared with proliferating cancer cells.

in protein levels. To further reinforce the increased sensitivity to inhibition of BCL2-family, cells undergoing INK128 persistence or senescence (for 7 days) were subsequently treated for 5 additional days with siRNA pools targeting BCL2, BCL-XL, or BCL-W (**Fig. 2D**; Supplementary Fig. S2E). Interestingly, si*BCL-XL*, but not si*BCL2* or si*BCL-W*, reduced the viability of senescent and persister

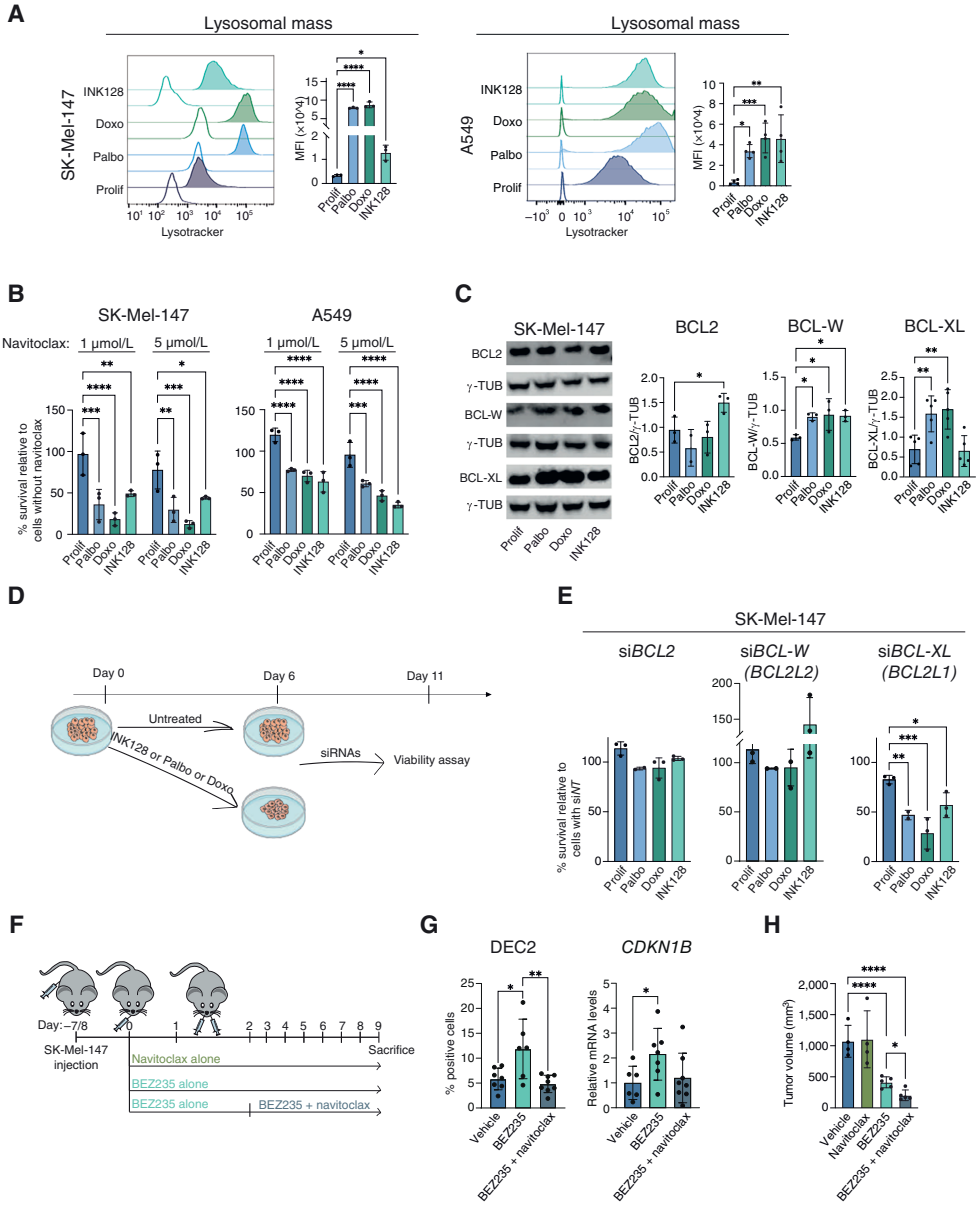

Figure 2.

Shared features between persister and senescent cancer cells. **A,** Flow cytometry analysis of LysoTracker Red in proliferating, senescent [palbociclib (palbo) and doxorubicin (doxo)], and persister (INK128) SK-Mel-147 and A549 cells. Representative histograms showing the fluorescence signal of each stained sample and its unstained control (uncolored histogram). Quantification of the mean fluorescence intensity (MFI) after autofluorescence subtraction ($n = 3$ SK-Mel-147; $n = 4$ A549). *, $P < 0.05$; **, $P < 0.01$; ***, $P < 0.001$; ****, $P < 0.0001$; one-way ANOVA compared with proliferating control cells. **B,** Crystal violet viability assay of proliferating, palbociclib-treated, doxorubicin-treated, and INK128-treated SK-Mel-147 and A549 cells after navitoclax treatment (72 hours) at 5 and 1 μmol/L. Percentage of survival was calculated in comparison to each respective untreated control ($n = 3$). Quantification was done using the Synergy HTX absorbance microplate reader. *, $P < 0.05$; **, $P < 0.01$; ***, $P < 0.001$; ****, $P < 0.0001$; two-way ANOVA compared with proliferating controls. **C,** BCL2, BCL-W, and BCL-XL and γ-tubulin protein levels in proliferating, palbociclib-treated, doxorubicin-treated, and INK128-treated SK-Mel-147 cells. A representative immunoblot is shown ($n = 3$ for BCL2 and BCL-W; $n = 5$ for BCL-XL). *, $P < 0.05$; **, $P < 0.01$; one-way ANOVA compared with proliferating controls. **D,** Schematic of the protocol used for siRNA transfection and viability assessment. **E,** CellTiter-Glo viability assay of proliferating, palbociclib-treated, doxorubicin-treated, and INK128-treated SK-Mel-147 cells treated with siRNAs targeting *BCL2*, *BCL-W* (*BCL2L2*), and *BCL-XL* (*BCL2L1*). Viability was assessed 5 days after siRNA transfection ($n = 3$). Raw data for quantification were acquired by measuring luminescence in a VICTOR Multilabel Plate Reader (PerkinElmer). *, $P < 0.05$; **, $P < 0.01$; ***, $P < 0.001$; one-way ANOVA compared with proliferating controls. **F,** Schematic of the cancer treatment protocol used in this study. **G,** Left, percentage of cells stained positive for DEC2 by IHC in vehicle, BEZ235, and BEZ235 + Navi tumors, at the end of the treatment (day 9; $n = 6$–8). Right, mRNA expression levels of *p27* (*CDKN1B*) in vehicle, BEZ235, and BEZ235 + Navi tumors at the end of the treatment (day 9), measured by qRT-PCR (relative to the average expression of housekeeping genes *ACTB* and *GAPDH*). *, $P < 0.05$; **, $P < 0.01$; one-way ANOVA compared with proliferating controls ($n = 6$–8). **H,** Tumor volume at sacrifice of SK-Mel-147 tumor-bearing animals treated with vehicle, navitoclax, BEZ235, and BEZ235 + navitoclax ($n = 4/5$). *, $P < 0.05$; ****, $P < 0.001$; two-way ANOVA analysis considering all the groups and all the days (for full graphs see Supplementary Fig. S4).

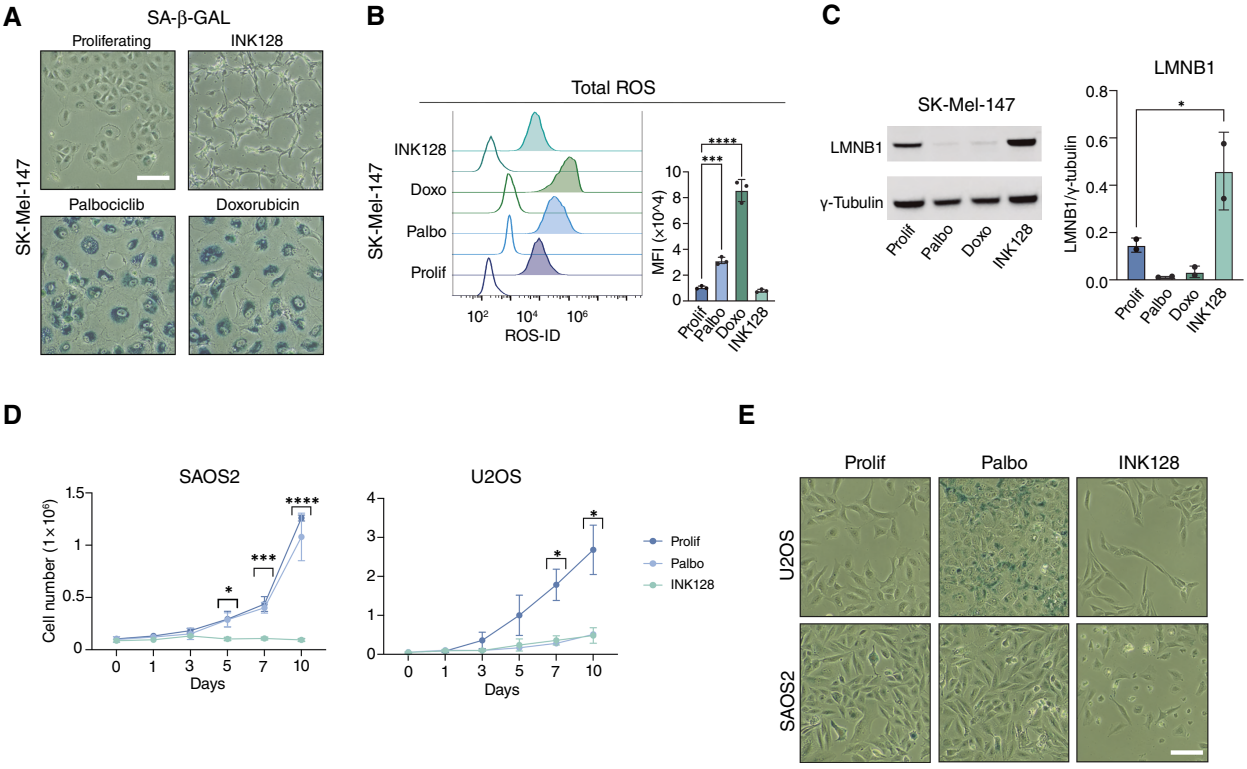

Figure 3.

Distinctive features between persister and senescent cancer cells. **A,** SA-β-GAL staining (blue) of proliferating, palbociclib-treated, doxorubicin-treated, and INK128-treated SK-Mel-147 after 7 days from the beginning of the treatment. **B,** Flow cytometry analysis of total ROS in proliferating, palbociclib (palbo)-treated, doxorubicin (doxo)-treated, and INK128-treated SK-Mel-147 cells. Representative histograms showing the fluorescence signal of each stained sample and its unstained control (uncolored histogram). Quantification of the mean fluorescence intensity (MFI) after autofluorescence subtraction ($n = 3$). ***, $P < 0.001$; ****, $P < 0.0001$; one-way ANOVA compared with proliferating control cells. **C,** LMNB1 and γ-tubulin protein levels in proliferating, palbociclib-treated, doxorubicin-treated, and INK128-treated SK-Mel-147 cells. A representative immunoblot is shown ($n = 2$). *, $P < 0.05$; one-way ANOVA compared with proliferating controls. **D,** Proliferation curve of SAOS2 and U2OS cells untreated (proliferating), treated with palbociclib (5 μmol/L) and treated with INK128 (100 nmol/L). Cells were counted using a hemocytometer after 24 hours from plating, 3, 5, 7, and 10 days ($n = 3$). *, $P < 0.05$; ***, $P < 0.001$; ****, $P < 0.0001$; multiple unpaired Student t test. **E,** SA-β-GAL staining (blue) of proliferating, palbociclib-treated, and INK128-treated SAOS2 and U2OS after 7 days from the beginning of the treatment. Scale bar, 50 μm.

SK-Mel-147 and A549 cells (**Fig. 2E**; Supplementary Fig. S2F). Given the efficacy of navitoclax in killing persister cells *in vitro*, we tested whether this drug could contribute to disease control *in vivo* using tumor xenografts treated with a clinical grade dual ATP-competitive mTOR/PI3K inhibitor, BEZ235 (also known as dactolisib). We injected athymic nude mice subcutaneously with SK-Mel-147 cells and when tumors reached approximately 100 mm^3 in size, we initiated treatment by oral gavage with BEZ235 (to induce persistence) and/or navitoclax for seven additional days (**Fig. 2F**). To confirm the induction of BEZ235-persistence in tumor xenografts, we examined the levels of markers DEC2 (by IHC) and *p27* (*CDKN1B*; by qRT-PCR; **Fig. 2G**; Supplementary Fig. S2G). Importantly, both markers were elevated in BEZ235-treated tumors compared with untreated ones, indicating the ability of the treatment to induce persistence *in vivo*. Interestingly, although navitoclax had no effect on tumor growth when used as single agent, it had a significant impact in reducing tumor growth when used in combination with BEZ235 (**Fig. 2H**; Supplementary Fig. S2H). Moreover, the reduction in the levels of both p27 and DEC2 after the combined treatment confirms the capability of navitoclax to target the persister population *in vivo*. Mice treated with the combination navitoclax and BEZ235 did not show signs of renal and liver toxicity, as assessed by serum markers (Supplementary Fig. S2I). We conclude that persister cancer cells are sensitive to BCL-XL inhibition, a feature that is shared with senescent cells.

Distinctive features between persister and senescent cancer cells

In contrast to the similarities reported above, when we analyzed SA-β-GAL activity, we detected increased levels only in senescent cells, but not in INK128-persister cells, an observation that was made in multiple cell lines (SK-Mel-147, A549, MCF7, MDA-MB-231, and H1299; **Fig. 3A**; Supplementary Fig. S3A). Elevated levels of total ROS are another feature of senescent cells. Notably, however, INK128-persister cells had total ROS levels comparable to those of proliferating cells and clearly lower than senescent cells (**Fig. 3B**; Supplementary Fig. S3B). Another hallmark of senescence is the loss of LMNB1, a component of the nuclear lamina, a feature that we confirmed in SK-Mel-147 and A549 senescent cells (**Fig. 3C**; Supplementary Fig. S3C). Interestingly, INK128-persister cells had increased levels of LMNB1 compared with proliferating and senescent

cells (**Fig. 3C**; Supplementary Fig. S3C). These distinctive features, namely, absence of SA-β-GAL activity, normal ROS, and preservation of LMNB1, add to the catalog of properties that distinguish persistence from senescence.

In an additional effort to define senescence and persistence, we asked whether a cell line incapable of entering senescence could still be able to enter persistence. For this, we used cell lines U2OS and SAOS2, two osteosarcoma cell lines that are distinguished by the functional status of the retinoblastoma gene (*RB1*) and, consequently, by their ability to undergo cellular senescence: U2OS are RB1 functional and can enter senescence in response to palbociclib, whereas SAOS2 cells lack functional RB1 and are incapable of entering senescence after palbociclib treatment, as we confirmed by measuring proliferative arrest and SA-β-GAL activity (**Fig. 3D** and **E**). Interestingly, both cell lines underwent efficient proliferative arrest upon exposure to INK128, accompanied by lack of SA-β-GAL. These results indicate that SAOS2 cells, despite being unable to enter senescence, still are capable of INK128-persistence. These observations reinforce the concept that senescence and persistence reflect distinct cell-cycle arrest programs.

Persister cancer cells lack a SASP

To gain deeper insight into the mechanistic differences between persister cells and senescent cells, we compared their transcriptional profiles. Specifically, we generated RNA-seq profiles of untreated, senescent (triggered by palbociclib and by doxorubicin), and persister (induced by INK128) SK-Mel-147 and A549 cells. Principal component analysis showed that each of these three states (proliferative, senescent, and persister) formed three clearly separated clusters (**Fig. 4A**; Supplementary Fig. S4A). When compared with proliferative cells, GSEA revealed a number of pathways that were differentially regulated between persister and senescent cells. The most notable ones were a group of pathways related to secretion and inflammation, which were upregulated only in senescent cells (**Fig. 4B**). There were no pathways selectively upregulated in persister cells, and only three pathways (WNT/βCAT, TGFβ, and SHH) were commonly upregulated in both persister and senescent cells. As expected, numerous pathways related to proliferation were commonly downregulated (**Fig. 4B**). Analysis by GSEA of a proteomic-based SASP signature of oncogene-induced senescence and radiation-induced senescence (43) confirmed the expected activation of the SASP in senescent cells; on the contrary, SASP signatures were repressed in persister cells (**Fig. 4C**). When focusing on individual SASP factors upregulated in SK-Mel-147 and A549 senescent cells, the large majority remained unchanged in SK-Mel-147 and A549 persister cells when compared with proliferating cells (Supplementary Fig. S4B and S4C). Importantly, the SASP signatures were also significantly absent in the published (24) transcriptional profiles of xenografts from human colorectal cancers undergoing irinotecan persistence, which was in contrast to xenografts that were untreated, recovered from therapy, or resistant to therapy (**Fig. 4D**). These results suggest that, in stark opposition to senescent cancer cells, the SASP is absent or even actively repressed in persister cancer cells.

Identification of genes specifically involved in the survival of persister cells

Based on our analysis of senescent versus persister cells, we concluded that these represent two related but fundamentally distinct cancer cell states. Thus, we reasoned that persister cancer cells may exhibit other vulnerabilities beyond their sensitivity to BCL2 family inhibition that could open novel approaches for tumor control. Capitalizing on the similarities between persister cancer cells and embryonic diapause, we performed a genetic screening in diapause mESCs designed to identify genes essential for the survival of diapause mESCs, but not for the survival of proliferating mESCs. By using mESCs, we aimed to avoid confounding factors related to the use of a specific cancer cell line, such as the presence of genetic mutations, aneuploidies that affect gene dosage, and particularities related to the tissue of origin. As detailed below, the resulting candidate survival genes for diapause mESCs were subsequently tested in human persister cancer cells. We used a previously described mESC line carrying a doxycycline-inducible Cas9 and an exome-wide single guide (sgRNA) library (30). These mESCs were treated with INK128 for 5 days to induce diapause, and doxycycline was then administered for 3 more days to trigger Cas9/sgRNA editing (**Fig. 5A**). A similar procedure was carried out on mESCs that were not treated with INK128, that is, in proliferating mESCs. The relative abundance of sgRNAs (ratio after versus before Cas9 induction) was obtained for diapause mESCs and for proliferating mESCs and those depleted by at least two-fold following Cas9 induction ($\log_2$ fold change ≤ -1.00) were selected for further analysis. In this manner, we identified 824 genes specific for the survival of diapause mESCs, 83 genes commonly involved in the survival of both diapause and proliferating mESC, and 229 genes specific for the survival of proliferating mESC (**Fig. 5B**; Supplementary Table S7).

We focused on the 824 genes specific for the survival of diapause cells. Encouragingly, we found that *Prdx1* (encoding PRDX1) was the gene with the highest sgRNA depletion in diapause cells, whereas *Prdx1* sgRNAs were not altered in proliferating mESC (**Fig. 5C**). Peroxiredoxin-1 (PRDX1) is an activator and downstream effector of NRF2 (encoded by *Nfe2l2*), a transcription factor reported to be critical for tumor dormancy (44). Consistent with the relevance of our mESC screen to human cancer cells, when *siPRDX1* was tested in INK128 persister cancer cells (SK-Mel-147 and A549), it also led to a reduction in their survival, whereas it had no effect on proliferating cells (Supplementary Fig. S5A). The abundance of *Nfe2l2* sgRNAs was also reduced specifically in diapause mESCs (Supplementary Fig. S5B), and its downregulation in INK128 persister SK-Mel-147 led to reduced survival (Supplementary Fig. S5B). These results validate the potential of our screening platform to identify diapause-specific survival genes and further confirm the existence of functional similarities between the states of murine embryonic diapause and human cancer cell persistence.

To discover novel mechanisms of survival specific to persister cancer cells, we performed pathway analysis of the 824 depleted survival candidate genes using the EnrichR software. This analysis highlighted once again the importance of the KEAP1/NRF2 pathway as a top vulnerability of diapause arrested cells (**Fig. 5D**). We were particularly interested in one-carbon (1C) metabolism, which was listed among the most significantly enriched pathways using several independent databases, including Reactome in which 1C metabolism was the top scored pathway (**Fig. 5D**; Supplementary Fig. S5C). The 1C metabolism comprises the methionine and folate cycles (**Fig. 5E**), which together shuttle methyl groups, mostly derived from serine and choline/betaine (45) to generate substrates important for multiple processes, including nucleotide biosynthesis, redox balance, and the methylation of both histones and DNA (45). Interestingly, several other enriched pathways also suggested that diapause cells are highly dependent on

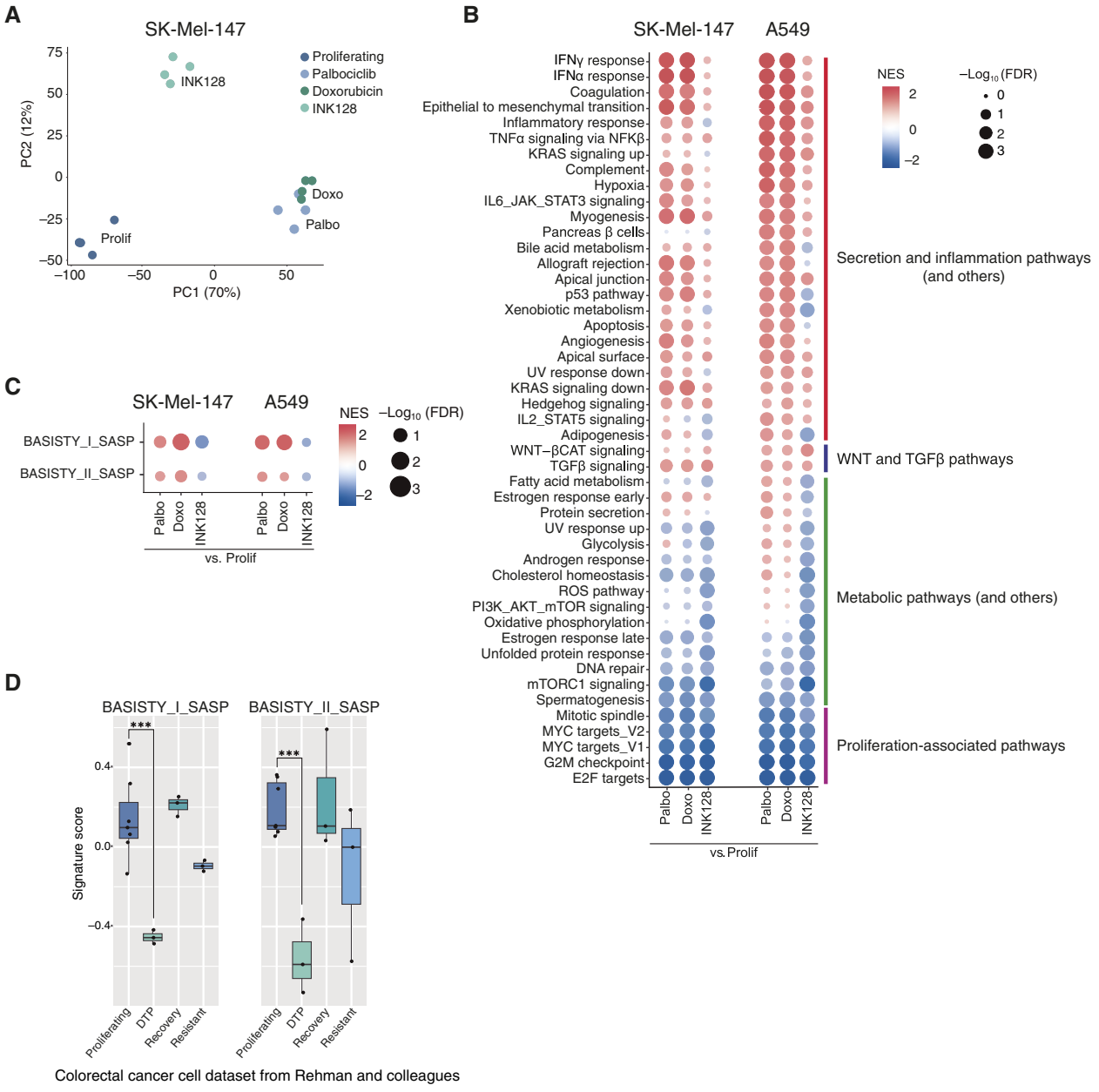

Figure 4.

Persister cancer cells lack a SASP. **A,** Principal component (PC) analysis of proliferating, palbociclib-treated, doxorubicin-treated, and INK128-treated SK-Mel-147 cells ($n = 4$). **B,** GSEA of palbociclib-treated, doxorubicin-treated, and INK128-treated vs. proliferating SK-Mel-147 and A549 cells. Only pathways significantly differentially regulated in SK-Mel-147 or A549 cells are represented. Normalized enrichment scores (NES) and $\log_{10}$ FDR are indicated. **C,** Dot plot summarizing the results of preranked GSEA analysis testing the differential enrichment of SASP gene sets (49) in palbociclib-treated, doxorubicin-treated, and INK128-treated vs. proliferating SK-Mel-147 and A549 cells. NES and $\log_{10}$ (FDR) are indicated. **D,** Signature scores of proliferating, DTP, recovery, and resistant colorectal cancer cells (published datasets from Rehman and colleagues, ref. 24) when interrogated for the expression of the SASP gene sets (proliferating, $n = 8$; all the other conditions, $n = 3$; ref. 49). ***, $P < 0.01$; one-way ANOVA compared with proliferating controls.

1C metabolism, such as cysteine and methionine metabolism (which feed 1C metabolism), cobalamin metabolism, and vitamin digestion (vitamins B6, B9, and B12 are critical cofactors for the methionine cycle), and the methionine *de novo* salvage pathway (**Fig. 5D**; Supplementary Fig. S5C). Indeed, diapause mESCs presented significant depletion of sgRNAs targeting genes involved in 1C metabolism and DNA methylation (*Bhmt*, *Mtr*, *Mat2a*, *Mtap*, *Tcn2*, *Ahcyl2*, *Dnmt1*, and *Uhrf1*; **Fig. 5E**, marked with a red dot), whereas the abundance of the same sgRNAs was not altered in proliferating mESC (**Fig. 5F**).

We tested the effect of the downregulation of some of these genes in proliferating, persister, and senescent human cancer cells. The

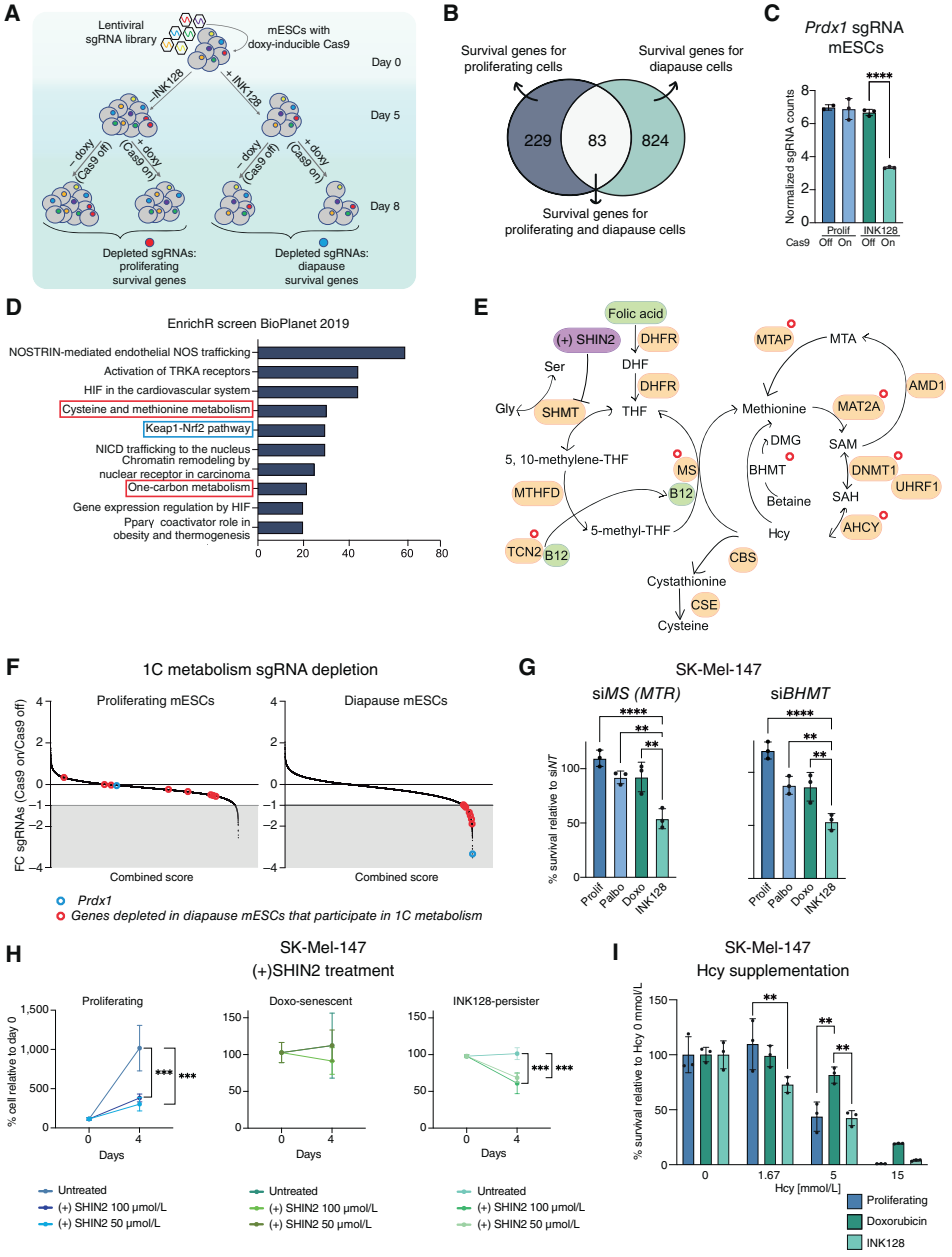

Figure 5.

Whole-genome CRISPR/Cas9 screen identifies 1C metabolism as a specific vulnerability of persister cancer cells. **A,** Schematic of the CRISPR/Cas9 screening experiment used in this study. **B,** Venn diagram displaying sgRNAs depleted in proliferating and diapause mESCs with a $\log_2$FC cutoff of −1. **C,** *Prdx1* sgRNA counts in proliferating and diapause mESCs untreated (Cas9 off) and treated (Cas9 on) with doxycycline (proliferating Cas9 off mESCs, $n = 2$; all the other conditions, $n = 3$). ****, $P < 0.0001$; one-way ANOVA vs. Cas9 off diapause mESC. **D,** Top 10 significantly enriched terms from EnrichR BioPlanet 2019 when analyzing the genes found depleted in the diapause mESCs treated with doxycycline. Combined score is performed using the EnrichR software by multiplying the log *P* value from the Fisher exact test by the *z*-score of the deviation from the expected rank. **E,** Schematic of the 1C metabolism. Red dots, the genes identified as depleted in the screen in diapause mESC. **F,** Representation of the $\log_2$FC of all the sgRNAs detected in the screen in proliferating mESC and diapause mESC (fold change of Cas9 on vs. Cas9 off for each condition). Red points, genes associated with 1C metabolism; blue point, *Prdx1*, the most depleted gene in the diapause mESC condition. **G,** CellTiter-Glo viability assay of proliferating, palbociclib (palbo)-treated, doxorubicin (doxo)-treated, and INK128-treated SK-Mel-147 cells transfected with si*MS* (*MTR*) and si*BHMT* for 5 days ($n = 3$ or 4). The percentage of survival was calculated in comparison to the respective si*NT*. Raw data for quantification were acquired by measuring luminescence in a VICTOR Multilabel Plate Reader (PerkinElmer). **, $P < 0.01$; ****, $P < 0.0001$; one-way ANOVA compared with proliferating controls. **H,** Cell count. Proliferating, doxorubicin-treated, and INK128-treated SK-Mel-147 cells (doxorubicin and INK128 treatments lasted 7 days) were counted before (day 0) or after 4 days of (+)SHIN2 treatment (50 and 100 μmol/L). Cells were counted using the CellDrop CellCounter (DeNovix). ***, $P < 0.001$; two-way ANOVA compared with cell count at day 0. **I,** CellTiter-Glo viability assay of proliferating and INK128-treated SK-Mel-147 cells with supplementation of homocysteine at three different concentrations: 1.67, 5, 15 mmol/L ($n = 3$). Viability was assessed 72 hours after Hcy supplementation. Raw data for quantification were acquired by measuring luminescence in a VICTOR Multilabel Plate Reader (PerkinElmer). **, $P < 0.01$; two-way ANOVA.

inclusion of senescent cells in these analyses was to discriminate whether the candidate survival genes represent persister-specific vulnerabilities or are shared between persister and senescent cancer cells. siRNA-mediated knockdown of *DNMT1*, *UHRF1*, *BHMT*, and *MTR* significantly reduced the survival of INK128-treated SK-Mel-147 but had no effect on proliferating cancer cells (**Fig. 5G**; Supplementary Fig. S5D–S5F). Senescent cancer cells were not sensitive to the knockdown of these genes, with the exception of si*DNMT1*, which produced a milder albeit significant reduction in survival (Supplementary Fig. S5F). Although most of the hits identified in diapause mESCs were validated in INK128-persister human SK-Mel-147 cells, there were some exceptions. For example, inhibition of *AHCYL2* had no effect on persister, senescent, or proliferating SK-Mel-147 cells (Supplementary Fig. S5F), perhaps due to compensation by the paralogs AHCY and AHCYL1. In the case of A549 cells, we could only validate a persister-specific survival role for *DNMT1* and *UHRF1* (Supplementary Fig. S5G). In an effort to recapitulate the dependency on 1C metabolism using a pharmacologic approach, we used (+)SHIN2, an inhibitor of serine hydroxymethyltransferase (SHMT), a key enzyme for the incorporation of methyl groups derived from serine into the 1C cycle. As expected (46), (+)SHIN2 treatment reduced the rate of proliferation in proliferating SK-Mel-147 cells (**Fig. 5H**). Interestingly, (+)SHIN2 led to a significant reduction in the total number of cells in INK128-persister cells, but not in senescent cells (**Fig. 5H**). We also tested the effects of homocysteine (Hcy), a metabolite that in excess is converted into S-adenosyl-homocysteine (SAH), a strong competitor of the universal methyl-donor S-adenosyl-methionine (SAM), thereby compromising methyltransferase reactions (47, 48). We observed that INK128-persister cancer cells were more sensitive to Hcy (1.67 mmol/L) than senescent or proliferating cells (**Fig. 5I**).

To substantiate the role of 1C metabolism in persister cells, we performed a targeted analysis of SAM and SAH. The SAM/SAH ratio is defined as the "methylation index" because it indicates the methylation capacity of a cell (49). We found that the SAM/SAH ratio was significantly increased in INK128-persister SK-Mel-147 cells compared with proliferating cells (Supplementary Fig. S5H), suggesting a higher methylation demand.

Collectively, the above data indicate that persister cells are more vulnerable to inhibition of 1C metabolism as compared with proliferating or senescent cancer cells, and this nominates pharmacologically actionable targets, such as the inhibition of SHMT, for the therapeutic elimination of persister cells.

Persister cancer cells present H4K20me3 heterochromatic foci

Based on the importance of 1C metabolism for epigenetic reactions, we looked at the levels of a variety of histone methylation marks involved in gene regulation. In particular, we tested a panel of H3 modifications (H3K9me3, H3K27me3, H3K4me3, and H3K4me1) and the H4 modification H4K20me3 in SK-Mel-147 cells. Immunoblot analysis revealed a modest but significant increase in H3K9me3 and H4K20me3 in both senescent and persister SK-Mel-147 cells compared with proliferating cells, whereas other marks, such as H3K27me3, H3K4me3, and H3K4me1 were unchanged (**Fig. 6A**; Supplementary Fig. S6A). In the case of A549 cells, we observed a clear increase in the levels of H4K20me3 in senescent and persister cells, whereas H3K9me3 was elevated in persister cells, but not in senescent cells (**Fig. 6B**). H3K9me3 and H4K20me3 are two canonical heterochromatin marks that have been implicated in quiescence (50, 51) and senescence (13–15, 52–54). The presence of high levels of H3K9me3 in senescent cells is highly variable depending on the cell type and senescence trigger (55). Elevated levels of H3K9me3 in persister cancer cells have been previously reported and linked to the silencing of repeated elements (23). In contrast, H4K20me3 remains unexplored in the context of cancer persistence. By immunofluorescence staining, proliferating cells presented a weak but diffuse H4K20me3 nuclear signal, whereas senescent and persister cells presented numerous nuclear foci of high intensity (**Fig. 6B**; Supplementary Fig. S6C). We examined the levels of the four known methyltransferases that generate H4K20me3, namely, KMT5B (SUV420H1), KMT5C (SUV420H2), SMYD3, and SMYD5 (56, 57). Interestingly, both *KMT5B* and *KMT5C* transcript levels were increased in senescent and persister SK-Mel-147 compared with proliferating cells, whereas the levels of *SMYD3* and *SMYD5* remained unchanged (**Fig. 6C**; Supplementary Fig. S6D). Interestingly, when persister cells resumed proliferation upon withdrawal of INK128, H4K20me3 levels returned to the same levels as in proliferating cells, as detected by immunoblot and immunofluorescence (**Fig. 6D** and **E**; Supplementary Fig. S6E). These observations suggest that persister cells, like senescent cells, undergo changes in the repressive heterochromatic mark H4K20me3.

Persister cancer cells present repressive H4K20me3 at promoters of inflammatory genes

To gain a more comprehensive understanding of the role of H3K9me3 and H4K20me3 in persister cells, we performed CUT&Tag for these epigenetic marks in proliferating, senescent, and persister SK-Mel-147 and A549 cells. To analyze the data, we used ChromHMM (58), which identifies recurrent configurations (called "states") of a given set of epigenetic marks (in our case H3K9me3 and H4K20me3) in an unbiased manner, across a set of samples. ChromHMM of SK-Mel-147 and A549 cells under the three conditions studied (proliferative, senescent, and persister) identified seven states with a differential configuration of these two histone marks. For each state, we report the emission probability, which is the probability of the presence of H3K9me3 and H4K20me3 in the different conditions analyzed. In the case of senescent cells, we observed notable changes in the abundance of H3K9me3 compared with proliferating cells (**Fig. 7A**). These changes consisted of both losses (states 1 and 2) and gains (states 4 and 6) in H3K9me3, compared with proliferating cells. In relation to this, previous reports have described remarkable changes in the localization of H3K9me3 associated with the loss of LMNB1 (13). In contrast, persister cells did not show alterations in the abundance of H3K9me3 across the different states defined by ChromHMM and compared with proliferating cells (**Fig. 7A**).

Analysis of the abundance of H4K20me3, on the other hand, revealed a number of chromatin states that gained this mark in persister and/or senescent cells. In particular, states 3, 5, and 6 were enriched in H4K20me3 in both conditions. Notably, state 7 was the only one in which persister cells behaved differently from both proliferating and senescent cells; specifically, this state was enriched in H4K20me3 in persister cells (**Fig. 7A**). When we interrogated the composition of genomic features in the above states, state 7 was the only one that contained a large proportion of promoter regions, whereas the remaining states were mainly composed of intergenic and intronic regions (Supplementary Fig. S7A). For illustrative purposes, we show two examples of promoters that gain H4K20me3 selectively in persister cancer cells compared with senescent or proliferating cells (**Fig. 7B**). Of note, simple repeats

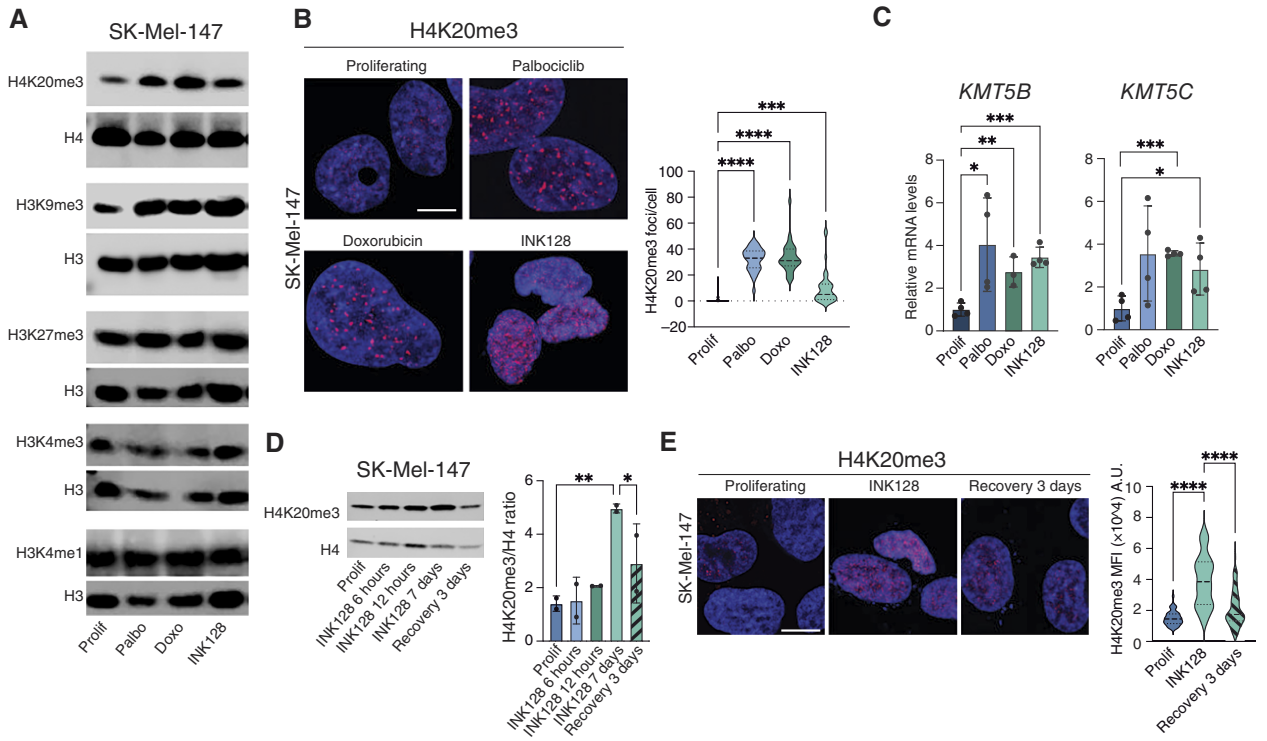

Figure 6.

Persister cancer cells present H4K20me3 foci. **A,** H4K20me3, total H4, H3K9me3, H3K27me3, H3K4me3, H3K4me1, and total H3 protein levels in proliferating, palbociclib (palbo)-treated, doxorubicin (doxo)-treated, and INK128-treated SK-Mel-147 cells. A representative immunoblot is shown ($n = 5$ for H4K20me3 and $n = 3$ for H3K9me3, H3K27me3, H3K4me3, and H3K4me1). Quantification in Supplementary Fig. S6. **B,** Immunostaining of H4K20me3 (red) and DAPI (blue) in proliferating, palbociclib-treated, doxorubicin-treated, and INK128-treated SK-Mel-147 cells. Scale bar, 10 μm. Right, quantification of foci per cell. ***, $P < 0.001$; ****, $P < 0.0001$; one-way ANOVA compared with proliferating controls. $n = 53$, proliferating; $n = 43$, palbociclib; $n = 38$, doxorubicin; $n = 44$, INK128. **C,** mRNA expression levels of *KMT5B* (*SUV420H1*) and *KMT5C* (*SUV420H2*) in untreated (proliferating) and INK128-treated SK-Mel-147 cells, measured by qRT-PCR (relative to the average expression of housekeeping genes *ACTB* and *GAPDH*). *, $P < 0.05$; ***, $P < 0.001$; unpaired Student *t* test, compared with proliferating controls ($n = 4$). **D,** H4K20me3 and total H4 protein levels in proliferating, INK128-treated (6 hours, 12 hours, 7 days) and INK128-recovery (7 days of INK128 treatment, folowed by 3 days of withdrawal) SK-Mel-147 cells. A representative immunoblot (left) and quantification (right) from $n = 2$ is shown. H4K20me3 levels were normalized on total H4 levels. *, $P < 0.05$; **, $P < 0.01$; one-way ANOVA compared with INK128 (7 days). **E,** Immunostaining of H4K20me3 (red) and DAPI (blue) of SK-Mel-147 cells in the following conditions: proliferating, INK128-treated, and cells after 3 days from INK128 withdrawal. Representative images are shown. Scale bar, 10 μm. Right, quantification of mean fluorescence intensity (MFI). ****, $P < 0.0001$; one-way ANOVA compared with INK128 (7 days). Cell numbers were $n = 46$ (proliferating), $n = 40$ (INK128), $n = 60$ (recovery 3 days).

and repeats of low complexity were the only type of repeats over-represented in state 7, and this was a distinctive feature of state 7 compared with all the other states (Supplementary Fig. S7B). In this regard, it is interesting to mention that H4K20me3 is known to be enriched not only in satellite repeats but also in simple and low complexity repeats (59, 60). We next interrogated whether the promoters in state 7 were enriched for genes in specific biological pathways. Remarkably, among the pathways enriched in state 7, some were related to secretory and inflammatory processes that were highly expressed in senescent cells but not in persister cells, such as the IFN pathways (**Fig. 7C**; Supplementary Fig. S7C). These data suggest that the differences in the transcriptional profiles between senescent and persister cancer cells can be associated with an increase in H4K20me3 in the promoters of genes related to inflammatory pathways.

To get a deeper understanding of the epigenetic differences present at IFN-regulated promoters between senescent and persister cells, we plotted the average profiles of H4K20me3 centered at promoters in the different conditions and cell lines. In senescent cells, IFN-regulated genes presented very low levels of H4K20me3 at their promoters, below the basal levels observed in proliferating cells. In contrast, persister cells showed enrichment or preservation of H4K20me3 (**Fig. 7D**). Consistent with the repressive role of H4K20me3 at promoters (61, 62), mRNA levels of individual IFN-regulated genes marked with H4K20me3 were downregulated in persister cells (**Fig. 7E**; Supplementary Fig. S7D; IFNα and IFNγ pathways, respectively). IFN signaling is a major inducer of antigen presentation by the MHC-I complex in senescent cells (34). We hypothesized that the lack of IFN activation in persister cells might result in the absence of MHC-I expression on the plasma membrane surface. We measured MHC-I levels on the plasma membrane of proliferating, senescent, and persister cells. As expected, both senescent SK-Mel-147 and A549 cells upregulated MHC-I, as detected by an antibody against HLA-A, -B, and -C (**Fig. 7F**; Supplementary Fig. S7E). In contrast to senescent cells, and in agreement with the H4K20me3 epigenetic data, INK128-persister cells did not show upregulation of MHC-I compared with proliferating cancer cells (**Fig. 7F**; Supplementary Fig. S7E).

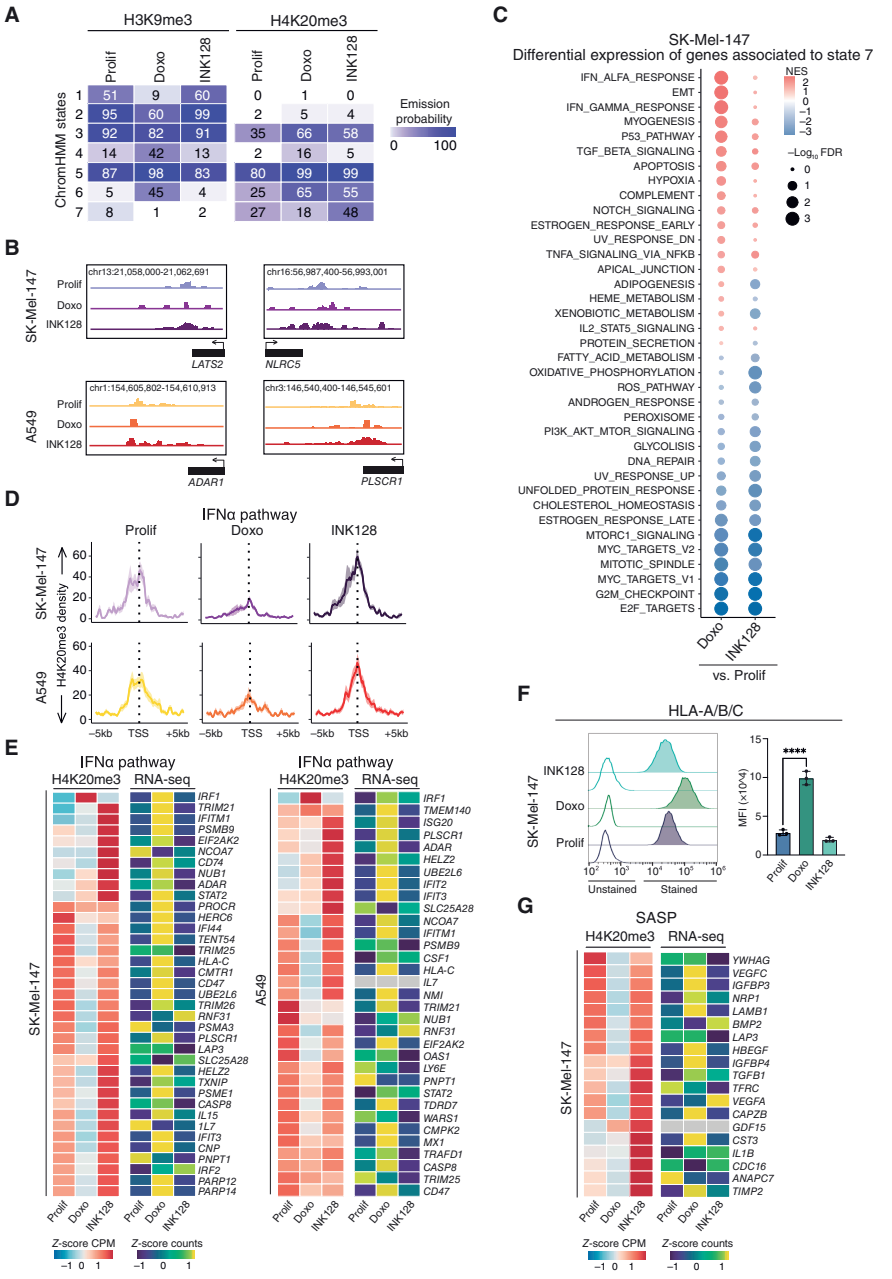

Figure 7.

H4K20me3 is differentially associated with IFN and SASP promoter regions in senescent and persister cancer cells. **A,** Heatmap summarizing the ChromHMM emission matrix of H3K9me3 and H4K20me3 over the ChromHMM states 1–7 in proliferating, doxorubicin (doxo)-treated, INK128-treated SK-Mel-147 and A549 cells ($n = 3$). **B,** Bigwigs of examples of promoter regions that exhibit increased H4K20me3 signal in chromatin from INK128-treated compared with proliferating and doxorubicin-treated SK-Mel-147 and A549 cells. **C,** Dotplots of preranked GSEA associated with the ChromHMM state 7 of SK-Mel-147 and A549 cells, where genes were ranked according to their fold change between treated and controls cells. Normalized enrichment score (NES) is color-coded, whereas statistical significance (FDR) is encoded in the size of the dots. **D,** H4K20me3 signal over promoters of genes in the GSEA hallmark gene sets related to IFNα pathway that intersect with ChromHMM state 7 in proliferating, doxorubicin-treated, INK128-treated A549 and SK-Mel-147 cells. **E,** Heatmaps plotting the levels of H4K20me3 over promoters in gene set "Hallmark interferon alpha response" that intersect with ChromHMM state 7 in proliferating, doxorubicin-treated, INK128-treated SK-Mel-147 and A549 cells. This is accompanied by a heatmap plotting the normalized RNA-seq counts for these genes, averaging replicates ($n = 4$). **F,** Flow cytometry analysis of human (HLA-A/B/C) MHC-I expression in proliferating, palbociclib-treated, doxorubicin-treated, and INK128-treated SK-Mel-147 cells. Representative histograms showing the fluorescence signal of each stained sample and its unstained control (uncolored histogram). Quantification of the mean fluorescence intensity (MFI) after autofluorescence subtraction ($n = 3$). ****, $P < 0.0001$; one-way ANOVA compared with proliferating control cells. **G,** Heatmaps plotting the levels of H4K20me3 over promoters of SASP genes (previously defined in Supplementary Fig. S4B) that intersect with ChromHMM state 7 in proliferating, doxorubicin-treated, and INK128-treated SK-Mel-147 cells. This is accompanied by a heatmap plotting the normalized RNA-seq counts for these genes, averaging replicates ($n = 4$).

Finally, we wondered if the absence of SASP in persister cells could be associated with the presence or absence of H4K20me3 at the promoter regions of SASP genes. Indeed, all the SASP promoter regions of senescent cells lost H4K20me3, consistent with their transcriptional activation. In contrast, persister cells retained or gained the repressive mark H4K20me3 at SASP promoters (**Fig. 7G**; Supplementary Fig. S7F). Collectively, these data reveal that the differential expression of inflammatory pathways (IFN response genes and SASP-encoding genes) between senescent and persister cells is associated with the absence or presence, respectively, of the repressive epigenetic mark H4K20me3.

Persister cells activate inflammatory programs upon inhibition of methyltransferases KMT5B/C

To address the causal implication of H4K20me3 in the repression of inflammatory genes in persister cells, we analyzed the effect of the downregulation of *KMT5B* and *KMT5C*, the methyltransferases responsible for H4K20 trymethylation. Combined siRNA-mediated downregulation of both *KMT5B* and *KMT5C* in INK128-persister SK-Mel-147 cells (7 days of treatment with INK128, followed by siRNA transfection and analysis 2 days later) led to an upregulation of the tested inflammatory genes compared with persister cells treated with nontargeting siRNAs (**Fig. 8A**; Supplementary Fig. S8A and S8B). Inhibition of individual

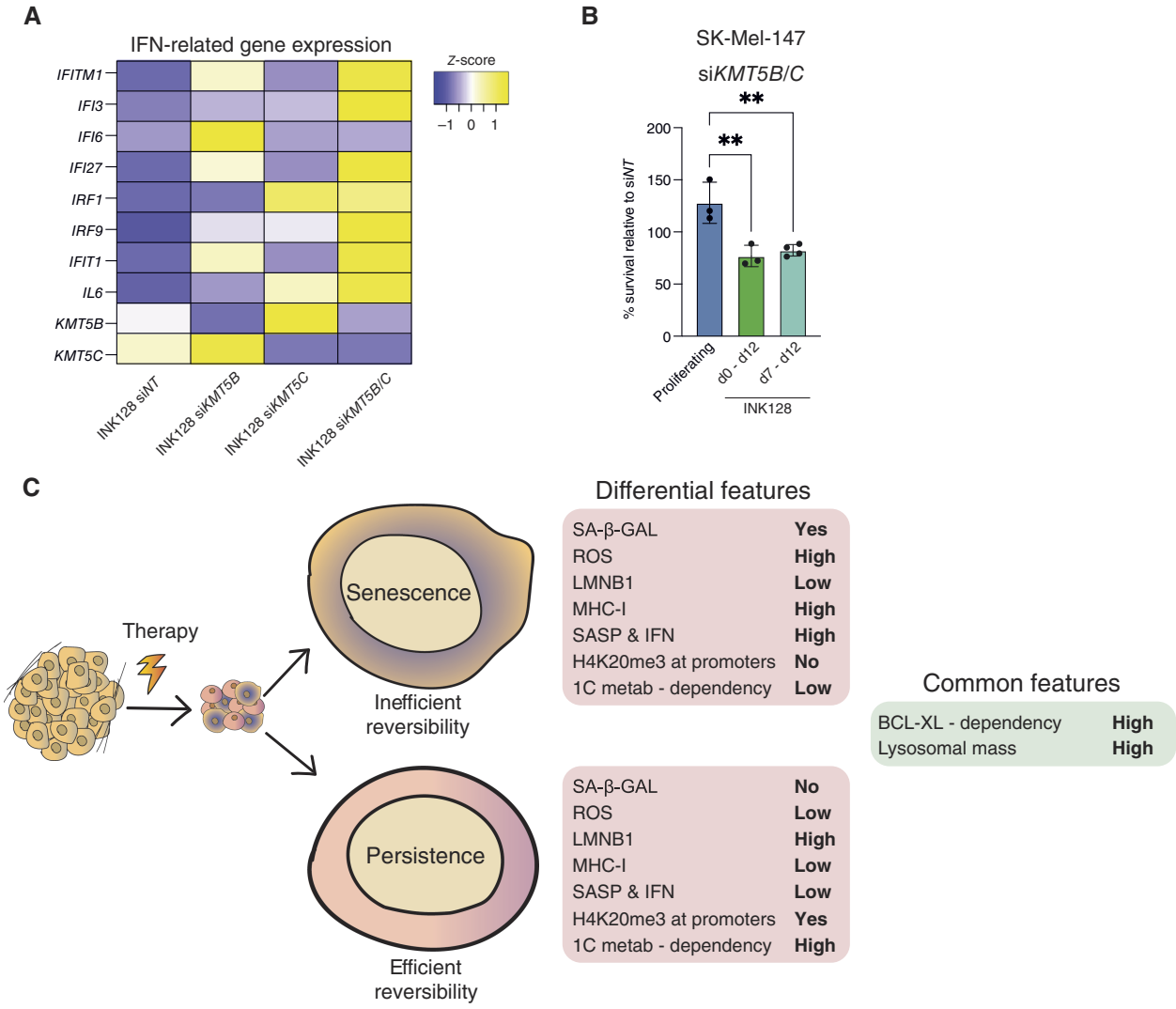

Figure 8.

Persister cancer cells activate inflammatory programs upon inhibition of methyltransferases KMT5B/C. **A,** Gene expression levels of IFN-related genes measured by qRT-PCR (relative to the average expression of housekeeping genes *ACTB* and *GAPDH*) of INK128-treated SK-Mel-147 cells transfected with si*NT*, si*KMT5B*, si*KMT5C*, and si*KMT5B/C* (7 days of treatment with INK128, followed by siRNA transfection and analysis 2 days later; $n = 4$). Please note that in the case of si*KMT5B/C*, only two replicates have been considered for further analysis, based on the efficiency of the silencing. **B,** Viability as measured by CellTiter-Glo assay of proliferating SK-Mel-147 cells transfected with si*KMT5B+C* for 5 days, SK-Mel-147 cells treated with INK128 and transfected at the same time with si*KMT5B/C* until the end of the assay at day 12 (d0–d12), and SK-Mel-147 cells treated with INK128 and transfected 7 days later with si*KMT5B+C* until day 12 (d7–d12; $n = 3$ or 4). The percentage of survival was calculated in comparison to the respective si*NT*. Raw data for quantification were acquired by measuring luminescence in a VICTOR Multilabel Plate Reader (PerkinElmer). **, $P < 0.01$; one-way ANOVA compared with proliferating controls. **C,** Graphical summary of the mechanism of differential inflammatory profiles in senescent and persister cancer cells. See text for details.

KMT5B or *KMT5C* had a milder effect, probably due to the compensatory upregulation of the remaining methyltransferase (**Fig. 8A**; Supplementary Fig. S8A and S8B). Combined inhibition of *KMT5B* and *KMT5C* also resulted in decreased survival of persister cells compared with proliferating cells treated with the same siRNAs (**Fig. 8B**). This was observed both when the siRNA transfection was done from the time of initiation of persistence with INK128 until the end of the assay (d0–d12), or when the transfection was done in INK128-persister cells established for 7 days until the end of the assay (d7–d12; **Fig. 8B**). These data demonstrate a crucial role of H4K20me3 in cancer cell persistence and in particular in the repression of inflammatory programs that are derepressed/activated in senescent cells.

Discussion

In this study, we characterize a model of drug-tolerant persister cancer cells driven by INK128, an ATP-competitive inhibitor of mTOR. We show that INK128-treated cancer cells present features of both persistence and tumor dormancy, and that their

transcriptional profile resembles embryonic diapause. This is consistent with emerging evidence highlighting the similarities between these three states of reversible arrest, namely, persistence, dormancy, and diapause (4, 24, 25).

The main distinctive feature between persister (including dormant and diapause) and senescent cells concerns the reversibility of these states. Persister cells efficiently resume proliferation after the conditions that triggered persistence are removed; this is not the case for senescent cells that generally have a low capacity of reversion due to the stability of the epigenetic, metabolic, and morphologic remodeling associated with senescence (63). In addition to this functional distinction, we define a number of cellular features that are differential between senescent and persister cancer cells (**Fig. 8C**). The senescence hallmarks that are absent in persister cells are the following: high SA-β-GAL activity, high levels of ROS, and loss of LMNB1 (**Fig. 8C**). Another important difference between persister and senescent cells derives from the finding that persister cells lack the SASP and the transcriptional programs associated with IFN signaling, including the absence of MHC-I upregulation, which could conceivably promote evasion of immunosurveillance (**Fig. 8C**).

Among the common traits between senescent and persister cancer cells is the expansion of the lysosomal compartment, which is likely attributable to their high autophagic activity (**Fig. 8C**; refs. 10, 24, 26). Interestingly, the SA-β-GAL activity, which is a lysosomal enzyme detected at a sub-optimal pH in senescent cells, was absent in persister cells, therefore disconnecting lysosomal expansion from SA-β-GAL. This is consistent with previous reports noting that SA-β-GAL activity in senescent cells is extinguished upon inhibition of mTOR activity (64, 65). Transcriptomic analysis revealed upregulation of the TGFβ and the WNT/βCAT pathways in both senescent and persister cancer cells; these pathways have been reported to be upregulated during tumor dormancy *in vivo* (36, 37). Another interesting trait shared by senescent and persister cells is their sensitivity to the BCL2 family inhibitor navitoclax, whose efficacy was attributable to the specific inhibition of BCL-XL in both types of cell-cycle arrest. To support this observation *in vivo*, we treated mice carrying human tumor xenografts with a dual ATP-competitive mTOR/PI3K inhibitor and/or with navitoclax. Interestingly, although navitoclax had no effect on tumor growth as a single agent, it significantly synergized with the dual mTOR/PI3K inhibitor. This suggests that persister cancer cells, like senescent cells, are pharmacologically targetable *in vivo* with navitoclax (**Fig. 8C**).

To identify additional vulnerabilities of persister cancer cells, we performed a CRISPR/Cas9 screen in mESCs, thus leveraging the similarities between diapause in embryonic cells and persistence in cancer cells. We identified *Prdx1* as the most depleted gene in diapause mESCs, and we validated *PRDX1* and its upstream transcriptional activator *NRF2* as survival genes also in our human cancer models of persistence. PRDX1 is one of the mediators of ROS detoxification by the master regulator NRF2 (66, 67), and NRF2 has been involved in the survival of dormant cells (44).

Unbiased pathway analysis of depleted genes specific to the diapause population also highlighted a possible hypersensitivity to the inhibition of 1C metabolism. The 1C metabolism is important for providing methyl groups in the form of SAM, which is used for biosynthetic processes and for the methylation of both histones and DNA (45). In particular, we identified the enzymes *BHMT* and *MTR*, both involved in separate reactions that generate methionine, as essential genes for persister SK-Mel-147 cells. In addition, we identified *DNMT1* and *UHRF1* as critical for the survival of persister SK-Mel-147 and A549 cells. Of note, UHRF1 is a binding partner and a critical cofactor of DNA methyltransferase DNMT1 (68–70). In support of the importance of methylation reactions, persister cells presented increased SAM/SAH ratios, which are indicative of higher methylation capacity. The identification of 1C metabolism as a critical vulnerability of persister cells opens the possibility to target these cells pharmacologically. In particular, we present proof of concept using (+)SHIN2, an inhibitor of SHMT, a critical enzyme that feeds methyl moieties derived from serine into the 1C metabolism (45, 46). Persister cell survival was compromised by treatment with (+)SHIN2, whereas this compound did not affect senescent cells and reduced the rate of proliferation in proliferating cells, as previously reported (46). Similarly, the survival of persister cancer cells was more affected by the presence of high concentrations of Hcy. High Hcy is known to cause both oxidative damage (71) and inhibition of methyltransferases, via the accumulation of SAH (47). Together, these data indicate that persister cells have a strong dependency on 1C metabolism for their survival, which makes then more sensitive to inhibitors of 1C metabolism compared with senescent or proliferative cells.

Based on the importance of 1C metabolism for histone methylation reactions, we looked at the levels of selected histone methylation marks. We detected a modest but significant global increase of both H3K9me3 and H4K20me3 in persister cancer cells by immunoblotting. Elevated H3K9me3 in models of persistence has already been reported (23); in contrast, to the best of our knowledge, there was no information on H4K20me3 in persister cancer cells. Interestingly, H4K20me3 foci were increased in both senescent and persister cells compared with proliferating cells, and the increased levels of this mark in persister cells returned to normal levels upon INK128 withdrawal.

To further characterize the role of H3K9me3 and H4K20me3 in senescent and persister SK-Mel-147 and A549 cancer cells, we performed CUT&Tag. These data revealed two important differences between senescent and persister cells. In regard to H3K9me3, this mark was largely unchanged in persister cells compared with proliferating cells, whereas in senescent cells, it underwent a partial relocalization that mostly affected intergenic and intronic elements. Relocalization of H3K9me3 in senescent cells does not have a clear impact on the transcriptional profile of senescent cells (72), and it has been connected to the loss of LMNB1 (13). In relation to this, it is relevant to mention here our observation that persister cells do not present loss of LMNB1.

In regard to the heterochromatic mark H4K20me3, we observed a different behavior in intergenic/intronic regions compared with promoter regions. In the case of intergenic/intronic regions, there was an increase in the abundance of this epigenetic mark observable both in senescent and persister cells, compared with proliferating cells. This elevation may be connected to the emergence of immunofluorescence-detectable H4K20me3 foci in senescent and persister cells. Interestingly, a group of promoter regions with low levels of H4K20me3 in proliferating cells showed a discrepant behavior between senescent and persister cells: senescent cells present a reduction of H4K20me3 at this group of promoters, whereas persister cells present an increase in the levels of this mark (**Fig. 8C**). Although H4K20me3 has been typically associated with constitutive heterochromatin in centromeres and telomeres (56), it can also be located at promoters and consequently play a role in silencing gene expression (61, 62, 73). Indeed, we observed that the promoter-rich regions that present H4K20me3 in persister cells have an overabundance of simple and low complexity repeats, which

are known to be marked by H4K20me3 (56, 59, 60). When we analyzed the biological functions associated with the genes whose promoters were differentially bound by H4K20me3 in persister and senescent cells, we found them to be related to inflammatory pathways, notably IFN-regulated genes and SASP genes. The loss of H4K20me3 in the promoters of inflammatory genes may underlie, at least in part, the upregulation of these pathways in senescent cells. Conversely, the gain of H4K20me3 provides an epigenetic explanation for the lack of SASP and IFN gene expression in persister cells. Interestingly, the lack of SASP expression in persister cells was confirmed by the analysis of a published dataset of xenografts of human colorectal cancers under irinotecan-tolerant persistence (24), further supporting the idea that the INK128-model of drug-tolerant persister cells recapitulates general features of persistence.

Finally, persister cells presented increased expression of *KMT5B* and *KMT5C*, two methyltransferases responsible for the trimethylation of H4K20. Concomitant silencing of both methyltransferases led to a derepression of inflammatory genes in persister cells and resulted in loss of survival compared with proliferating cancer cells, confirming the crucial role of H4K20me3 in cancer cell persistence and unraveling another vulnerability of this cell population. Although we do not exclude that other mechanisms could influence the expression of inflammatory genes, our data strongly suggest that the presence of H4K20me3 at the promoters is key for the repression of these genes, independently of other regulatory mechanisms.

In summary, we provide a characterization of distinct and shared features between senescent and persister cancer cells. Importantly, we used a CRISPR/Cas9-based screen to identify actionable vulnerabilities of persister cells; the results of this screen uncovered epigenetic insights into the regulation of the SASP and the inflammatory state, which is absent in persister cells (**Fig. 8C**). These findings, including our conserved persister transcriptional signature and the unique vulnerabilities that we have identified, could be instrumental for the study of these cells in post-therapy tumors *in vivo*, particularly in single-cell analyses. We speculate that heterogeneous proportions of senescent and persister cells could influence the microenvironment, the immune infiltration of the tumor and the likelihood of relapse. Moreover, we do not exclude the possibility that manipulation of persister cells could lead to their entry into the senescent state. Further studies are warranted to understand the interplay between both states and how each contributes to minimal residual disease and tumor relapse.

Authors' Disclosures

M. Kovatcheva reports personal fees from mesoestetic and Galapagos outside the submitted work. A.E. Lord reports grants and personal fees from Barry Reed Fund outside the submitted work. M. Serrano reports grants from AECC during the conduct of the study, as well as other support from Altos Labs, Inc, Rejuversen, AG, Senolytic Therapeutics, SL, Life Biosciences, Inc., and grants from Galapagos, NV outside the submitted work. No disclosures were reported by the other authors.

Authors' Contributions

V. Ramponi: Conceptualization, formal analysis, investigation, methodology, writing–original draft, writing–review and editing. **L. Richart:** Conceptualization, data curation, software, formal analysis, writing–original draft, writing–review and editing. **M. Kovatcheva:** Conceptualization, formal analysis, supervision, validation, investigation, methodology, writing–original draft, writing–review and editing. **C. Stephan-Otto Attolini:** Data curation, software, methodology. **J. Capellades:** Investigation. **A.E. Lord:** Conceptualization, investigation, methodology. **O. Yanes:** Conceptualization, resources, supervision, funding acquisition, investigation, methodology. **G. Ficz:** Conceptualization, formal analysis, supervision, funding acquisition, validation, writing–original draft, writing–review and editing. **M. Serrano:** Conceptualization, resources, formal analysis, supervision, funding acquisition, validation, writing–original draft, writing–review and editing.

Acknowledgments

We are grateful to the Institute for Research in Biomedicine (IRB) Functional Genomics Unit and CRG/CNAG for library preparation and genomic sequencing, and to the IRB microscopy unit. V. Ramponi was recipient of a predoctoral contract from H2020-MSCA-ITN-2018 HealthAge Program. M. Kovatcheva was funded by the Barcelona Institute of Science and Technology, Asociación Española Contra el Cáncer (POSTD18020SERR), and the European Molecular Biology Organization. A.E. Lord was funded by The Barry Reed Fund. A.E. Lord and G. Ficz were funded by the Barts Cancer Institute. Work in the laboratory of M. Serrano was funded by the IRB and by a Coordinated-Asociación Española Contra el Cáncer grant (PRYCO211023SERR).

Note

Supplementary data for this article are available at Cancer Research Online (http://cancerres.aacrjournals.org/).

Received February 15, 2024; revised July 28, 2024; accepted October 25, 2024; published first October 30, 2024.

References

1. De Conti G, Dias MH, Bernards R. Fighting drug resistance through the targeting of drug-tolerant persister cells. Cancers (Basel) 2021;13:1118.
2. Wang B, Kohli J, Demaria M. Senescent cells in cancer therapy: friends or foes? Trends Cancer 2020;6:838–57.
3. Cabanos HF, Hata AN. Emerging insights into targeted therapy-tolerant persister cells in cancer. Cancers 2021;13:2666.
4. Vallette FM, Olivier C, Lézot F, Oliver L, Cochonneau D, Lalier L, et al. Dormant, quiescent, tolerant and persister cells: four synonyms for the same target in cancer. Biochem Pharmacol 2019;162:169–76.
5. Montagner M, Sahai E. In vitro models of breast cancer metastatic dormancy. Front Cell Dev Biol 2020;8:37.
6. Aguirre-Ghiso JA. Translating the science of cancer dormancy to the clinic. Cancer Res 2021;81:4673–5.
7. Hernandez-Segura A, Nehme J, Demaria M. Hallmarks of cellular senescence. Trends Cell Biol 2018;28:436–53.
8. Gorgoulis V, Adams PD, Alimonti A, Bennett DC, Bischof O, Bishop C, et al. Cellular senescence: defining a path forward. Cell 2019;179:813–27.
9. Biran A, Zada L, Abou Karam P, Vadai E, Roitman L, Ovadya Y, et al. Quantitative identification of senescent cells in aging and disease. Aging Cell 2017;16:661–71.
10. Tan JX, Finkel T. Lysosomes in senescence and aging. EMBO Rep 2023;24:e57265.
11. Dimri GP, Lee X, Basile G, Acosta M, Scott G, Roskelley C, et al. A biomarker that identifies senescent human cells in culture and in aging skin in vivo. Proc Natl Acad Sci U S A 1995;92:9363–7.
12. Höhn A, Weber D, Jung T, Ott C, Hugo M, Kochlik B, et al. Happily (n)ever after: aging in the context of oxidative stress, proteostasis loss and cellular senescence. Redox Biol 2017;11:482–501.
13. Sadaie M, Salama R, Carroll T, Tomimatsu K, Chandra T, Young ARJ, et al. Redistribution of the Lamin B1 genomic binding profile affects rearrangement of heterochromatic domains and SAHF formation during senescence. Genes Dev 2013;27:1800–8.
14. Narita M, Nuñez S, Heard E, Narita M, Lin AW, Hearn SA, et al. Rb-mediated heterochromatin formation and silencing of E2F target genes during cellular senescence. Cell 2003;113:703–16.
15. Shah PP, Donahue G, Otte GL, Capell BC, Nelson DM, Cao K, et al. Lamin B1 depletion in senescent cells triggers large-scale changes in gene expression and the chromatin landscape. Genes Dev 2013;27:1787–99.
16. Birch J, Gil J. Senescence and the SASP: many therapeutic avenues. Genes Dev 2020;34:1565–76.

17. Faget DV, Ren Q, Stewart SA. Unmasking senescence: context-dependent effects of SASP in cancer. Nat Rev Cancer 2019;19:439–53.
18. Chaib S, López-Domínguez JA, Lalinde-Gutiérrez M, Prats N, Marin I, Boix O, et al. The efficacy of chemotherapy is limited by intratumoral senescent cells expressing PD-L2. Nat Cancer 2024;5:448–62.
19. Chaib S, Tchkonia T, Kirkland JL. Cellular senescence and senolytics: the path to the clinic. Nat Med 2022;28:1556–68.
20. Wang L, Lankhorst L, Bernards R. Exploiting senescence for the treatment of cancer. Nat Rev Cancer 2022;22:340–55.
21. Sharma SV, Lee DY, Li B, Quinlan MP, Takahashi F, Maheswaran S, et al. A chromatin-mediated reversible drug-tolerant state in cancer cell subpopulations. Cell 2010;141:69–80.
22. Álvarez-Varela A, Novellasdemunt L, Barriga FM, Hernando-Momblona X, Cañellas-Socias A, Cano-Crespo S, et al. Mex3a marks drug-tolerant persister colorectal cancer cells that mediate relapse after chemotherapy. Nat Cancer 2022;3:1052–70.
23. Guler GD, Tindell CA, Pitti R, Wilson C, Nichols K, KaiWai Cheung T, et al. Repression of stress-induced LINE-1 expression protects cancer cell subpopulations from lethal drug exposure. Cancer Cell 2017;32:221–37.e13.
24. Rehman SK, Haynes J, Collignon E, Brown KR, Wang Y, Nixon AML, et al. Colorectal cancer cells enter a diapause-like DTP state to survive chemotherapy. Cell 2021;184:226–42.e21.
25. Dhimolea E, De Matos Simoes R, Kansara D, Al'Khafaji A, Bouyssou J, Weng X, et al. An embryonic diapause-like adaptation with suppressed myc activity enables tumor treatment persistence. Cancer Cell 2021;39:240–56.e11.
26. Li Y, Chen H, Lu D, Koeffler HP, Zhang Y, Yin D. Mitophagy is a novel protective mechanism for drug-tolerant persister (DTP) cancer cells. Autophagy 2023;19:2618–9.
27. Zhang Z, Tan Y, Huang C, Wei X. Redox signaling in drug-tolerant persister cells as an emerging therapeutic target. EBioMedicine 2023;89:104483.
28. Saudemont A, Quesnel B. In a model of tumor dormancy, long-term persistent leukemic cells have increased B7-H1 and B7.1 expression and resist CTL-mediated lysis. Blood 2004;104:2124–33.
29. Bulut-Karslioglu A, Biechele S, Jin H, Macrae TA, Hejna M, Gertsenstein M, et al. Inhibition of mTOR induces a paused pluripotent state. Nature 2016;540:119–23.
30. Ruiz S, Mayor-Ruiz C, Lafarga V, Murga M, Vega-Sendino M, Ortega S, et al. A genome-wide CRISPR screen identifies CDC25A as a determinant of sensitivity to ATR inhibitors. Mol Cell 2016;62:307–13.
31. Llanos S, Megias D, Blanco-Aparicio C, Hernández-Encinas E, Rovira M, Pietrocola F, et al. Lysosomal trapping of palbociclib and its functional implications. Oncogene 2019;38:3886–902.
32. Fan X, He Y, Wu G, Chen H, Cheng X, Zhan Y, et al. Sirt3 activates autophagy to prevent DOX-induced senescence by inactivating PI3K/AKT/mTOR pathway in A549 cells. Biochim Biophys Acta Mol Cell Res 2023;1870:119411.
33. Jochems F, Thijssen B, Conti GD, Jansen R, Pogacar Z, Groot K, et al. The Cancer SENESCopedia: a delineation of cancer cell senescence. Cell Rep 2021;36.
34. Marin I, Boix O, Garcia-Garijo A, Sirois I, Caballe A, Zarzuela E, et al. Cellular senescence is immunogenic and promotes antitumor immunity. Cancer Discov 2023;13:410–31.
35. Yang X, Wu J, Li M, Zhang W, Gao X, Wang H, et al. Inhibition of DEC2 is necessary for exiting cell dormancy in salivary adenoid cystic carcinoma. J Exp Clin Cancer Res 2021;40:169.
36. Bragado P, Estrada Y, Parikh F, Krause S, Capobianco C, Farina HG, et al. TGF-β2 dictates disseminated tumour cell fate in target organs through TGF-β-RIII and p38α/β signalling. Nat Cell Biol 2013;15:1351–61.
37. Ren D, Dai Y, Yang Q, Zhang X, Guo W, Ye L, et al. Wnt5a induces and maintains prostate cancer cells dormancy in bone. J Exp Med 2018;216:428–49.
38. Scognamiglio R, Cabezas-Wallscheid N, Thier MC, Altamura S, Reyes A, Prendergast ÁM, et al. Myc depletion induces a pluripotent dormant state mimicking diapause. Cell 2016;164:668–80.
39. Nicolas AM, Pesic M, Engel E, Ziegler PK, Diefenhardt M, Kennel KB, et al. Inflammatory fibroblasts mediate resistance to neoadjuvant therapy in rectal cancer. Cancer Cell 2022;40:168–84.e13.
40. Kurz DJ, Decary S, Hong Y, Erusalimsky JD. Senescence-associated β-galactosidase reflects an increase in lysosomal mass during replicative ageing of human endothelial cells. J Cell Sci 2000;113:3613–22.
41. Lee BY, Han JA, Im JS, Morrone A, Johung K, Goodwin EC, et al. Senescence-associated β-galactosidase is lysosomal β-galactosidase. Aging Cell 2006;5:187–95.
42. Zhu Y, Tchkonia T, Fuhrmann-Stroissnigg H, Dai HM, Ling YY, Stout MB, et al. Identification of a novel senolytic agent, navitoclax, targeting the Bcl-2 family of anti-apoptotic factors. Aging Cell 2016;15:428–35.
43. Basisty N, Kale A, Jeon OH, Kuehnemann C, Payne T, Rao C, et al. A proteomic atlas of senescence-associated secretomes for aging biomarker development. PLoS Biol 2020;18:e3000599.
44. Fox DB, Garcia NMG, McKinney BJ, Lupo R, Noteware LC, Newcomb R, et al. NRF2 activation promotes the recurrence of dormant tumour cells through regulation of redox and nucleotide metabolism. Nat Metab 2020;2:318–34.
45. Ducker GS, Rabinowitz JD. One-carbon metabolism in Health and disease. Cell Metab 2017;25:27–42.
46. García-Cañaveras JC, Lancho O, Ducker GS, Ghergurovich JM, Xu X, da Silva-Diz V, et al. SHMT inhibition is effective and synergizes with methotrexate in T-cell acute lymphoblastic leukemia. Leukemia 2021;35:377–88.
47. Kerr SJ. Competing methyltransferase systems. J Biol Chem 1972;247:4248–52.
48. Barroso M, Handy DE, Castro R. The link between hyperhomocysteinemia and hypomethylation: implications for cardiovascular disease. J Inborn Errors Metab Screen 2017;5:232640981769899.
49. Bravo AC, Aguilera MNL, Marziali NR, Moritz L, Wingert V, Klotz K, et al. Analysis of S-adenosylmethionine and S-adenosylhomocysteine: method optimisation and profiling in healthy adults upon short-term dietary intervention. Metabolites 2022;12:373.
50. Evertts AG, Manning AL, Wang X, Dyson NJ, Garcia BA, Coller HA. H4K20 methylation regulates quiescence and chromatin compaction. Mol Biol Cell 2013;24:3025–37.
51. Boonsanay V, Zhang T, Georgieva A, Kostin S, Qi H, Yuan X, et al. Regulation of skeletal muscle stem cell quiescence by suv4-20h1-dependent facultative heterochromatin formation. Cell Stem Cell 2016;18:229–42.
52. Schleich K, Kase J, Dörr JR, Trescher S, Bhattacharya A, Yu Y, et al. H3K9me3-mediated epigenetic regulation of senescence in mice predicts outcome of lymphoma patients. Nat Commun 2020;11:3651.
53. Sati S, Bonev B, Szabo Q, Jost D, Bensadoun P, Serra F, et al. 4D genome rewiring during oncogene-induced and replicative senescence. Mol Cell 2020;78:522–38.e9.
54. Nelson DM, Jaber-Hijazi F, Cole JJ, Robertson NA, Pawlikowski JS, Norris KT, et al. Mapping H4K20me3 onto the chromatin landscape of senescent cells indicates a function in control of cell senescence and tumor suppression through preservation of genetic and epigenetic stability. Genome Biol 2016;17:158.
55. Kosar M, Bartkova J, Hubackova S, Hodny Z, Lukas J, Bartek J. Senescence-associated heterochromatin foci are dispensable for cellular senescence, occur in a cell type- and insult-dependent manner and follow expression of p16 ink4a. Cell Cycle 2011;10:457–68.
56. Agredo A, Kasinski AL. Histone 4 lysine 20 tri-methylation: a key epigenetic regulator in chromatin structure and disease. Front Genet 2023;14:1243395.
57. Lin F, Zhang R, Shao W, Lei C, Ma M, Zhang Y, et al. Structural basis of nucleosomal H4K20 recognition and methylation by SUV420H1 methyltransferase. Cell Discov 2023;9:1–13.
58. Ernst J, Kellis M. ChromHMM: automating chromatin-state discovery and characterization. Nat Methods 2012;9:215–6.
59. Ozturk N, Dansranjavin T, Gies S, Calay D, Shiplu S, Creppe C, et al. H4K20me3 marks distal intergenic and repetitive regions in human mature spermatozoa. Development 2021;148:dev196477.
60. Hussain S, Sadouni N, van Essen D, Dao LTM, Ferré Q, Charbonnier G, et al. Short tandem repeats are important contributors to silencer elements in T cells. Nucleic Acids Res 2023;51:4845–66.
61. Xu J, Kidder BL. H4K20me3 co-localizes with activating histone modifications at transcriptionally dynamic regions in embryonic stem cells. BMC Genomics 2018;19:514.
62. Abbas T, Shibata E, Park J, Jha S, Karnani N, Dutta A. CRL4Cdt2 regulates cell proliferation and histone gene expression by targeting PR-Set7/Set8 for Degradation. Mol Cell 2010;40:9–21.
63. Reimann M, Lee S, Schmitt CA. Cellular senescence: neither irreversible nor reversible. J Exp Med 2024;221:e20232136.
64. Herranz N, Gallage S, Mellone M, Wuestefeld T, Klotz S, Hanley CJ, et al. mTOR regulates MAPKAPK2 translation to control the senescence-associated secretory phenotype. Nat Cell Biol 2015;17:1205–17.
65. Laberge R-M, Sun Y, Orjalo AV, Patil CK, Freund A, Zhou L, et al. MTOR regulates the pro-tumorigenic senescence-associated secretory phenotype by promoting IL1A translation. Nat Cell Biol 2015;17:1049–61.

66. Kim Y-J, Ahn J-Y, Liang P, Ip C, Zhang Y, Park Y-M. Human prx1 gene is a target of Nrf2 and is up-regulated by hypoxia/reoxygenation: implication to tumor Biology. Cancer Res 2007;67:546–54.
67. Tang C, Yin G, Huang C, Wang H, Gao J, Luo J, et al. Peroxiredoxin-1 ameliorates pressure overload-induced cardiac hypertrophy and fibrosis. Biomed Pharmacother 2020;129:110357.
68. Bostick M, Kim JK, Estève P-O, Clark A, Pradhan S, Jacobsen SE. UHRF1 plays a role in maintaining DNA methylation in mammalian cells. Science 2007;317:1760–4.
69. Mancini M, Magnani E, Macchi F, Bonapace IM. The multi-functionality of UHRF1: epigenome maintenance and preservation of genome integrity. Nucleic Acids Res 2021;49:6053–68.
70. Sharif J, Muto M, Takebayashi S, Suetake I, Iwamatsu A, Endo TA, et al. The SRA protein Np95 mediates epigenetic inheritance by recruiting Dnmt1 to methylated DNA. Nature 2007;450:908–12.
71. Balint B, Jepchumba VK, Guéant J-L, Guéant-Rodriguez R-M. Mechanisms of homocysteine-induced damage to the endothelial, medial and adventitial layers of the arterial wall. Biochimie 2020;173:100–6.
72. Chandra T, Kirschner K, Thuret J-Y, Pope BD, Ryba T, Newman S, et al. Independence of repressive histone marks and chromatin compaction during senescent heterochromatic layer formation. Mol Cell 2012;47:203–14.
73. Stender JD, Pascual G, Liu W, Kaikkonen MU, Do K, Spann NJ, et al. Control of proinflammatory gene programs by regulated trimethylation and demethylation of histone H4K20. Mol Cell 2012;48:28–38.